Master's thesis

NTNU
Norwegian University of Science and Technology
Faculty of Engineering
Department of Geoscience and Petroleum

Henriette Solhaug Lorentsen

The effect of streamer feathering on seismic data

Master's thesis in Petroleum Geosciences and Engineering
Supervisor: Børge Arntsen
June 2019

NTNU
Kunnskap for en bedre verden

Henriette Solhaug Lorentsen

The effect of streamer feathering on seismic data

Master's thesis in Petroleum Geosciences and Engineering
Supervisor: Børge Arntsen
June 2019

Norwegian University of Science and Technology
Faculty of Engineering
Department of Geoscience and Petroleum

NTNU
Norwegian University of
Science and Technology

Acknowledgement

This thesis was written at the Department of Geoscience and Petroleum (IGP) at the Norwegian University of Science and Technology (NTNU), in the spring of 2019.

I would like to thank my supervisor, Professor Børge Arntsen, for outstanding supervision and support throughout the project. He has always been available for questions and excellent guidance.

I am also grateful for the support and patience from my husband Torstein and our children Mathias, Emma, Johanne and Martine during the work of this thesis.

Trondheim, June 2019
Henriette Solhaug Lorentsen

Abstract

When a seismic streamer is exposed to crosscurrents during a 2D towed-streamer seismic survey, the planned 2D survey will turn into a limited swath 3D survey. Instead of a regularly sampled 2D midpoint distribution, streamer side drift yields a midpoint distribution irregularly scattered around the ship track. Ignoring the 3D character of the recorded data by applying a standard 2D processing scheme can result in deleterious effects as mis-ties or crossline smearing on the migrated images. A solution to this problem is to apply 3D migration to feathered data due to its 3D character. The goal of this thesis is to show that improved imaging can be achieved by treating feathered 2D seismic data as 3D seismic data.

Synthetic data is generated to simulate a feathered towed-streamer survey and a regular towed-streamer survey. The feathered survey is inspired by a towed-streamer survey acquired offshore Japan in 1999. The survey was severely feathered due to strong crosscurrents. By comparing 2D and 3D migrated images of the feathered case, we show that improved imaging accuracy can be achieved by taking into account the 3D character of feathered data. We also show that 3D migration of feathered data can turn feathering into an advantage, instead of a drawback. Three-dimensional geologic structures located outside the acquisition plane contribute to the total recorded data during a 2D seismic survey. It is hard to distinguish in-plane and out-of plane reflections on a 2D section and 2D imaging is not able to correctly migrate out-of plane reflections due to lack of crossline information. By applying 3D migration to feathered data, we achieve increased imaging accuracy as out-of plane reflections can be adequately processed and imaged.

Sammendrag

Når en seismisk kabel blir eksponert for sterke havstrømmer i løpet av en 2D seismisk undersøkelse, blir den planlagte 2D undersøkelsen isteden til en 3D seismisk undersøkelse med begrenset dekning. Kablene drives sidelengs bort fra innsamlingslinjen på grunn av havstrømmene som fører til en midpunkt distribusjon spredt rundt innsamlingslinjen, i stedet for en regelmessig innsamlet 2D midpunkt distribusjon langs innsamlingslinjen. Ved å prosessere de innsamlede datane med standard 2D prosesserings metoder, ser man bort fra 3D karakteristikken til datasettet noe som kan resultere i uheldige effekter som *mis-ties* eller *crossline smearing*. En løsning på problemet kan være å prosessere de innsamlede dataene med tanke på 3D karakteristikken ved å bruke 3D migrasjon. Målet med denne masteroppgaven er å vise at man kan oppnå forbedret imaging ved å behandle data samlet inn under en 2D *feathered* undersøkelse som om det var data samlet inn under en 3D undersøkelse.

Vi genererer data for å simulere en *feathered* undersøkelse og en regulær tauet-streamer undersøkelse. Den drifta undersøkelsen er inspirert av en undersøkelse utført utenfor Japan hvor kablene ble alvorlig sidedriftet på grunn av sterke havstrømmer. Ved å sammenligne 2D og 3D migrerte bilder av den driftede undersøkelsen, viser vi at det er mulig å oppnå forbedret nøyaktighet ved å ta hensyn til 3D karakteristikken til de driftede dataene. Vi viser også at drifting av kabler ikke bare er en hindring som må rettes, men kan gjøres om til en fordel med riktig håndtering av dataene. Seismiske bølger reflektert av tredimensjonale geologiske strukturer lokalisert utenfor innsamlings-tverrsnittet bidrar til den totale energien samlet inn under en 2D undersøkelse. For data som er samlet inn i 2D er det vanskelig å skille refleksjoner som stammer fra innsamlings-tverrsnittet fra refleksjoner som strammer fra geologiske strukturer lokalisert utenfor tverrsnittet. Dette er fordi data samlet inn i 2D ikke inneholder informasjon som er nødvendig for å migrere refleksjonene tilbake der dem hører hjemme. Ved å 3D migrere *feathered* seismisk data, oppnår vi forbedret nøyaktighet siden refleksjoner fra utenfor tverrsnittet blir adekvat prosessert og framstilt.

Table of Contents

List of Figures

List of Tables

Chapter 1

Introduction

Streamer feathering is the deviation of streamers from the desired acquisition track due to the presence of crosscurrents during a seismic marine towed-streamer survey. Varying sea conditions, as direction and strength of the sea currents, within a survey area can result in feathering varying from a few degrees to 30 degrees or more for one survey. The consequence is a midpoint distribution irregularly scattered around the ship track which turns the desired 2D survey into a limited swath 3D survey. Ideally, the midpoint distribution is a straight line with zero crossline width. The resulting 3D data set from a feathered 2D survey is characterized by uneven trace fold, irregular midpoint distribution and highly variable source-receiver azimuth. Ignoring the crossline offset during processing can yield deleterious effects as mis-ties or deviation in traveltimes (Kalra, 1986; Levin, 1983, 1984). It is therefore important to take into account the receiver crossline offset when processing feathered seismic data to assure high imaging accuracy.

Time-lapse studies are used to assess changes in the subsurface by analysing seismic data acquired at different times over the same area. This requires high repeatability of acquisition geometry as irregularly sampled data, for instance due to feathering, can lead to non-production related time-lapse differences. To ensure a high level of repeatability when seismic data is sampled, methods as steered-streamer acquisition, permanent seabed array acquisition or multiple streamer acquisition configuration have proven to give good results (Cooper et al., 1999; Eiken et al., 2003; Goto et al., 2004). Seismic data regularization methods can increase repeatability in cases where seismic data have been acquired with low repeatability. For data sampled at a regular grid, sinc interpolation in time-space domain can increase the repeatability between two surveys. Eiken et al. (2003) shows that applying a crossline interpolation scheme based on the Fourier transform to data acquired by multiple streamers with narrow separation can reduce the degree of nonrepeatability between surveys. Fourier reconstruction is applicable to irregularly sampled data as it can be formulated as an inverse problem. Signal estimated in the Fourier domain is transformed to a regular grid in the spatial domain by an inverse fast Fourier transform. This method requires no prior subsurface information.

It exist other regularization techniques based on the Fourier transform. Fourier recon-

struction with a sparse inversion (FRSI) approach in three spatial dimensions incorporates a nonquadratic penalty function in the inversion algorithm and allows for reconstruction of nonuniformly sampled, aliased seismic data in three or four spatial dimensions (Zwartjes and Gisolf, 2006). Marine seismic data are sampled in four spatial coordinates, the in-line and crossline coordinates of the source and receivers. Usually, the crossline shot coordinate is rather under sampled, while feathering often cause the hydrophone coordinates to be nonuniformly sampled. The FRSI method is divided in two steps. First, a 1D sinc interpolation is applied to reposition the hydrophones to a uniform in-line midpoint spacing. Then, a 3D Fourier reconstruction is applied to the crossline midpoint, absolute offset and azimuth coordinates to regularize the data. This method requires overlap shooting to assure azimuth multiplicity as the azimuth coordinate is included in the Fourier reconstruction.

To reduce the effect of feathering on seismic data, another data regularization method called crossline-offset interpolation is applicable (Gulick et al., 2004). Due to feathering, large areas of a 3D volume acquired offshore Japan required shot kills. Reshooting was performed to fill the large holes caused by the shot kill which produced an uneven offset distribution in some common depth point (CDP) bins after sorting and binning. The data was therefore sorted into gathers consisting of the common offsets in each crossline before a trace interpolation was applied to generate an even offset distribution across the survey. Landrø et al. (2019) used a 3D interpolation method based on Shepard's algorithm (Shepard, 1968) to increase repeatability between two surveys. The surveys were acquired offshore Japan before and after the 2011 Tohoku-Oki earthquake. Both surveys were feathered due to strong crosscurrents. The interpolation scheme increased the repeatability enough to enable time-lapse studies.

Seismic tomography is another tool for data regularization. Vesnaver et al. (2003) mitigates the effect of feathering by a 3D tomographic inversion algorithm. A tomographic grid adequate for all vintages is chosen before velocities and interfaces are estimated independently for each vintage. Then, the interface structures are averaged into one model. The velocities are also averaged across vintages, except for areas where the velocity is expected to vary across vintages. Finally, updated traveltimes can be calculated separately for each vintage. The use of a common initial model reduces the effect of mispositioning errors.

By extracting 3D structural information from 2D feathered seismic data it is possible to exploit the effect of feathering. Nedimović et al. (2003) shows how improved imaging can be achieved by taking into account the 3D character of feathered data. This is done by an optimum cross-dip stack procedure. True source and receiver positions and an improved normal moveout (NMO) equation whit an additional cross-dip moveout-term (CDMO) allows for local variation of cross-dip along the processing line. This method is applicable for models with moderate reflector dips and mild, lateral velocity variations. Nedimović suggest the use of 3D prestack migration to further improve imaging of feathered data. This requires an accurate velocity model which may not be possible to achieve as the sampling of 3D limited swath data rarely are dense enough in crossline-direction.

The main objective of this paper is to investigate the possibility of applying 3D prestack migration to 2D feathered marine seismic data to improve imaging accuracy of feathered data. We believe that a feathered 2D survey is indeed a 3D survey and should be treated as such. This approach is tested with synthetic data inspired by realistic bathymetry and

acquisition geometry from the feathered seismic marine survey *MY101* from Tohoku-Oki offshore Japan. We compare the method to nominal 2D migration of the feathered synthetic data as well as 3D migrated data generated to simulate a regular acquisition geometry (zero crossline-offset). We derive a new shot-profile imaging condition (Arntsen, 2019) which gives true amplitude angle gathers. Further, improved imaging resolution is gained with the novel imaging condition compared to the imaging condition given by Claerbout (1971).

Chapter 2

Theory

Images of geological structures of the Earth's subsurface can be created by seismic imaging using wave propagation theory. A wavefield induced by a seismic source propagates downwards into the subsurface. It gives rise to a reflected wave when it arrives at an interface between different geological units or a scattering point. The reflected waves are recorded at the surface and are used as input in seismic imaging methods. Given an accurate approximation of the physical properties of the subsurface, wavefield propagation can be predicted on a given velocity model by a set of linear equations describing wave propagation. Velocity analysis is normally used to obtain an appropriate background velocity model. A migrated image of the subsurface is produced by applying an imaging condition to the predicted wave propagation.

The recorded data set depends on subsurface properties, as well as the acquisition configuration. Common for all surveys is that a seismic signal is generated by a seismic source and recorded by receivers. How the signal is generated and recorded can vary from one survey to another. A survey can be a simple 2D survey, or a complex 3D survey. Seismic data can be acquired both onshore and offshore. Only marine seismic surveys will be considered in this paper as the focus is on seismic data acquired with feathered streamers.

To understand the effect of cable feathering, a comprehension on how the recorded seismic data depends on the acquisition configuration is necessary. Knowledge on how seismic migration works is also necessary as the accuracy of the output image depends on both how the seismic data is recorded and processed. The following sections first gives an introduction to seismic acquisition, then the theory behind seismic migration is presented.

2.1 Marine Seismic Acquisition

The goal of a seismic acquisition survey is to acquire data that can be processed into a subsurface image of the survey area. The main components common for all marine surveys are a seismic source and receivers. Depending on the objective of the survey, the

design of the acquisition set-ups can differ in type of source and receiver, source-receiver configuration, and the density of the acquired data.

The most conventional method is the towed streamer configuration. The seismic source and streamer(s) equipped with hydrophones are towed, close to the surface, behind a seismic vessel. Pressure waves (P-waves) only are generated at each shot point as the seismic source normally is a sound source as well as the fact that water is an acoustic media where only P-wave propagation occur. Furthermore, the signal recorded close to the surface will also consist of purely P-waves .

In ocean bottom seismic, receiver cables placed at the seabed are equipped with both hydrophones and geophones. The hydrophones record pressure changes, while the geophones record the velocity of the particle displacement. As the cables are places at the seabed, it is possible to record shear-waves (S-waves), as well as P-waves. Although the seismic source only generates P-waves, these P-waves can convert to S-waves when they enter the rigid subsurface due to mode-conversion. Compared to a conventional towed-streamer method, this method is more suitable to image complex areas due to the additional recorded information.

Vertical seismic profile (VSP) surveys involve lowering geophones into a well hole and recording the seismic signal generated by a source at the surface. The recorded seismic data during a VSP survey is commonly used to correlate geology interpreted from the well logs and seismic data from the site surveys. Feathered seismic data can only be obtained in a towed-streamer survey. Therefore, the following subsections will give a more detailed description of this method only.

2.1.1 Towed streamer acquisition

As previously mentioned, a towed-streamer acquisition configuration consists of towing both the source(s) and streamer(s) behind a seismic vessel. A number of shot points are evenly placed along the acquisition track, also called in-line direction. Between each shot point, source and receivers are relocated in order to increase the covered area.

Depending on the objective of the survey, towed-streamer methods can be divided into three main categories; 2D, 3D and 4D seismic surveys. In 2D towed streamer surveys, a single streamer and the source is towed behind the seismic vessel. The data recorded along a processing line is assumed to be reflections from reflectors or scattering points situated in the cross-section below the processing line. 2D seismic surveys are mostly used in frontier exploration areas in order to get an overall understanding of the geology of the area. Typically, several, parallel 2D lines separated by a few kilometers are acquired.

3D seismic surveys are used to locate geological structures that are likely to contain hydrocarbons in exploration seismic, or to monitor production of a reservoir. During a 3D survey, the seismic signal from one or two seismic sources are recorded by a number of streamers towed by the seismic vessel. Compared to a 2D survey, a 3D survey gives increased coverage in the direction perpendicular to the acquisition track, known as crossline direction. A typical 3D survey consists of dual source and 8-16 streamers separated by less than $100\,m$ in crossline direction (Dondurur, 2018). It also exists a number of complex 3D towed-streamer acquisition configurations such as multi-azimuth and wide-azimuth surveys. Multi-azimuth data is achieved by acquiring 3D data in multiple directions over the same area. A regular 3D configuration is presumed to be narrow-azimuth. Wide-azimuth

data is acquired by employing multiple vessels along crossline direction to increase the recording area.

3D surveys acquired over the same area at different times are called 4D surveys or time-lapse surveys. Time-lapse surveys are mostly used to assess hydrocarbon production in a reservoir over time. Changes in the subsurface due to production are small and require high repeatability between surveys to be adequately evaluated.

2.1.2 Seismic source

The most common used marine seismic source is the airgun. When an airgun is fired, the energy from releasing compressed air from an internal chamber is converted into sound waves. The volume of the internal chamber is used to describe the capacity of an airgun, usually given in cubic inches. Usually, an array of 18-48 airguns is used (Dondurur, 2018). For an airgun array, the capacity is proportional to the number of airguns. The source signal generated by an airgun array is both repeatable and possible to model.

The source tow depth is limited to a few metres to prevent the effect of the source ghost reflection. When a seismic source is fired, it gives rise to a wavefield that can be decomposed into a downgoing wavefield and an upgoing wavefield. The upgoing wavefield, called source ghost, is almost perfectly reflected by the sea surface. As the reflection coefficient of the sea surface is ≈ 1, the reflected signal is almost equal to the initial signal, but has opposite polarity. The source ghost arrives almost at the same time as the primary signal and with almost the same amplitude, but with opposite polarity.

2.1.3 Seismic streamer

A seismic streamer consists of a number of hydrophone groups located at a regular interval along a long cable. Hydrophone groups are usually located $12.5\,m$ or $25\,m$ apart. The length of a streamer usually varies between $3000\,m$ to $12000\,m$ in length, depending on the depth and type of the target.

Depth controls units, called birds, are used to control the tow depth of the streamer. It is important to tow the streamer deep enough to shield it from the weather. At the same time, it is important not to tow the streamer too deep in order to limit the receiver ghost effect. The receiver ghost effect is equivalent to the source ghost effect, see 2.1.2. Part of the primary signal is reflected by the sea surface above the streamer and arrives shortly after the primary signal, but with opposite polarity.

The streamer is flexible and in the presence of currents, the streamer will side drift in a curved shape (Krail and Brysk, 1989). For processing purposes, it is necessary to know the exact location of the hydrophones. Magnetic compasses are installed on some of the birds which, in combination with GPS data systems on the seismic vessel, can be used to calculate the true receiver coordinates as well as the feathering angle and the source coordinates.

2.1.4 Streamer feathering

As mentioned earlier, streamer feathering is when the streamer deviates from the desired acquisition track due to crosscurrents, this is shown in Figure 2.1. Instead of following

the ship track, the streamer makes an angle to the ship track, called feathering angle. As the streamer is flexible, it deviates from the ship track in a curved shape (Krail and Brysk, 1989). Accurate streamer positions, as well as shot locations, are calculated from navigation data collected during the seismic survey. These data include ship location, source location and data from compasses located along each streamer.

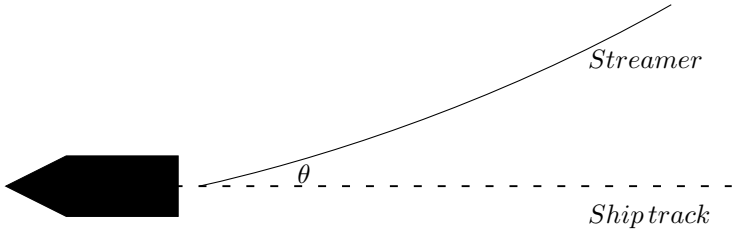

Figure 2.1: Illustration of streamer feathering. The streamer deviates from the ship track by an angle θ called feathering angle.

One of the consequences of streamer deviation is misplaced midpoints. The point on the surface halfway between the source and the receiver is called midpoint, see Appendix B. Ideally, during a 2D marine survey the streamer follows the ship track perfectly and all midpoints lie on the ship track. In the presence of feathering, the midpoints are scattered around the ship track. Crosscurrents normally cause the streamer to side drift to one side of the ship track which causes midpoint scattering on one side of the ship track only. If the direction and strength of crosscurrents varies within a survey area, midpoints are scattered to both sides of the ship track.

Misplaced midpoints can cause problems when shot gathers are sorted into common midpoint (CMP) gathers. A CMP is a midpoint shared by a number of source-receiver pairs with variable offsets. When the midpoints are scattered, there are no real CMPs (Levin, 1983). Figure 2.2 shows a simple example of a feathered survey. Receivers with related midpoints are plotted for several shot points. The midpoints are scattered to one side of the ship track and no real CMPs are present. One common approach to address this problem is to apply nominal 2D straight-line geometry where the crossline-offset is disregarded (Levin, 1984; Nedimović et al., 2003). Midpoints that lie on a common line perpendicular to the processing line are assigned, or binned, to a nominal CMP situated on the processing line. The midpoints assigned to a nominal CMP do not share a CMP, nor do they fall on the nominal CMP. In Figure 2.2, two points each fall on the lines perpendicular to the ship track. The points that fall on a common line perpendicular to the processing line will be assigned to a common nominal CMP although they do not share a midpoint nor do they fall on the nominal CMP. If the reflector is dipping, the midpoint is not situated vertically above the reflection point. Instead, the reflection point is moved updip from the point vertically below the midpoint, see Appendix B. As a consequence, in the case of a feathered streamer and a dipping reflector, the midpoint will not lie on the processing line, nor will it reflect the subsurface below the true midpoint.

Levin used a rather simple example to explain the effects of binning feathered data by applying nominal 2D straight-line geometry. The considered example consists of a single dipping reflector. In that case, if the shooting is done in dip direction, all midpoints within

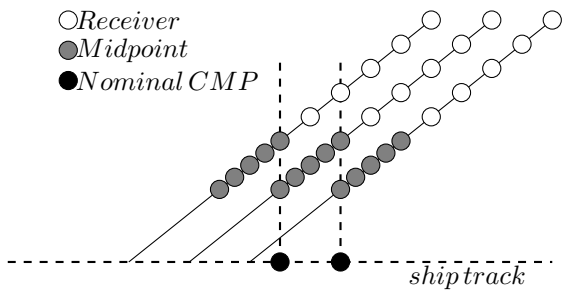

Figure 2.2: Simple illustration of a feathered survey. Receiver positions with associated midpoints are shown for several feathered streamers. Notice how there are no CMPs, nor does the midpoints fall on the shiptrack or the nominal CMPs.

a bin, or common perpendicular line, fall along strike. All midpoints along a strike line are the same distance from the reflector and the zero-offset traveltime will be equal for all traces. Levin shows that for a feathering angle of 30 degrees and a 15 degree reflector dip, pronounced traveltime errors occur only for large source-receiver offsets. In the case of shooting along strike direction, midpoints within a bin are not the same distance from the reflector. The zero-offset traveltimes will therefore vary for midpoints within a bin and corrections have to be made before binning. Levin therefore recommends that all seismic lines are shot in dip direction.

Levins approach is unrealistically simple and presumes that lateral variations of the subsurface are associated with dip and strike lines. This is seldom the case. Although the subsurface can have a predominant dip direction, it is often complex and contain 3D structures of variable shape, dip and orientation which causes lateral variations along both in-line and crossline directions. This means that even though seismic lines are shot in dip direction, the zero-offset traveltimes for midpoints associated with a nominal CMP can vary. It is therefore important to account for misplaced midpoints in the case of feathered streamers, regardless of the shooting direction.

Streamer fethering and traveltime errors

The traveltime t, from source to receiver via a reflection point, for a dipping reflector is given by

$$t = \sqrt{t_0^2 + \left(\frac{x}{v_{nmo}}\right)^2}, \tag{2.1}$$

where x is the distance between the source and the receiver, also called offset; t_0 is the zero-offset traveltime, or two-way vertical traveltime given by $t_0 = 2z/v$ with z the distance to the reflector and v the velocity; and v_{nmo} is the dip dependent apparent stacking velocity (Levin, 1971). See Appendix B for further details.

Traveltime errors due to misplaced midpoints can occur for a dipping reflector because of depth variations. The stacking velocity depend on local dip variations and misplaced midpoints can therefore yield stacking velocity errors if the dip varies locally for a reflector. The zero-offset traveltime will also be affected by misplaced midpoints as the depth to

the reflector can vary locally . The zero-offset traveltime error can be described as (Landrø et al., 2019)

$$\Delta t_0 = \frac{2\Delta z}{v_{nmo}}, \tag{2.2}$$

where Δz is the depth difference. If the local dip variations are small, the traveltime errors due to misplaced midpoints will only depend on zero-offset traveltime errors due to misplaced midpoints. The traveltime error Δt can then be given as (Landrø et al., 2019)

$$\Delta t = \frac{t_0}{t}\Delta t_0 + \frac{x}{t v_{nmo}^2}\Delta x. \tag{2.3}$$

An error in traveltime will not give a direct time-shift error on the migrated image, instead it will yield an error in stacking velocity Δv_{nmo} which again will cause a slightly unfocused image. The stacking velocity error Δv_{nmo} due to traveltime error can be written as (Landrø et al., 2019)

$$\Delta t = -\frac{1}{t}\frac{x^2}{v_{nmo}^3}\Delta v_{nmo}. \tag{2.4}$$

2.2 Migration

The objective of migration is to process the recorded seismic data into an image by focusing the reflected energy at its true subsurface location. The first step is to model, or simulate, wave propagation. In two-way wavefield extrapolation, the modeling is done in reverse-time by propagating the recorded reflected wavefield, or scattered wavefield, backward in time. At the same time, the source wavefield, or incident wavefield, is simulated forward in time. Given an algorithm able to accurately predict wavefield propagation, the two wavefield should meet perfectly at a reflection point. The next step is to apply an imaging condition in order to provide estimates of the reflection coefficients. A cross-correlation imaging condition involving zero-lag temporal correlation of the two wavefields is nonzero only for points where the two wavefields coincide, ideally at the true scattering point. Finally, an image is obtained by mapping the reflection coefficients for each time step.

One well known imaging condition is Claerbout's imaging condition (Claerbout, 1971). Wavefield extrapolation combined with Claerbout's imaging condition is widely used with both natural passive sources on a global scale as well as active sources on an exploration scale. Claerbout's imaging condition is stable and can easily be implemented numerically, but it is not able to estimate correct reflectivity in terms of Amplitude-Versus-Angle (AVA) information nor gives it an optimum resolution. The behavior of a wave when it is reflected by a reflector or a scattering point depends on the subsurface reflection coefficients, as well as the angle of incidence. In a feathered survey, the source-receiver offset is highly variable. The recorded data is therefore extremely AVA dependent. In order to compare 2D and 3D migration of feathered 2D seismic marine data, it is important to have a dynamically correct imaging condition that leads to correct AVA behavior. The novel imaging condition presented here is a modified version of Claerbout's imaging condition which gives true AVA behavior. It gives the correct reflectivity for data generated with point sources, as well as increased resolution compared to Claerbout's imaging condition

(Arntsen, 2019). The imaging condition is therefore well suited for studying the the effect of cable feathering.

2.2.1 True amplitude imaging condition for reverse time migration

The theory for the novel imaging condition is developed here. Feathered data is acquired in water which is an acoustic medium. As only pressure waves propagate in water, the theory will be developed with regards to pressure wave propagation only. The propagation of pressure waves are governed by the equation of motion (2.5) and Hooke's law (2.6):

$$\rho(\mathbf{x})\partial_t v_i(\mathbf{x},t) = \partial_i p(\mathbf{x},t) \tag{2.5}$$

$$\partial_t p(\mathbf{x},t) = \kappa(\mathbf{x})\partial_i v_i(\mathbf{x},t) + h(t)\delta(\mathbf{x}-\mathbf{x_s}). \tag{2.6}$$

where $\mathbf{x} = (x, y, z)$ is the spatial position; t is the time; ρ is the density; p is the acoustic pressure; κ is the bulk modulus; v_i is the particle velocity in direction i; $i = (x, y, z)$; δ is the Dirac delta function and h is the source pulse; $\mathbf{x_s}$ is the location of the source. The relation between the bulk modulus $\kappa(\mathbf{x})$ and the P-wave velocity $c(\mathbf{x})$ is given as $c(\mathbf{x}) = \sqrt{\kappa(\mathbf{x})/\rho(\mathbf{x})}$.

A background model is used to describe wave propagation within a given model without the interaction with a scattering point. The acoustic background pressure p_0 is described by the background velocity c_0. Here, an approximation to the background model is assumed to be known.

During a seismic experiment, when a source is fired it gives rise to a pressure wavefield. The wavefield can be decomposed into two parts. The first wavefield is the direct wave which propagates directly to the receivers. The second wavefield propagates downward into the subsurface until it reaches a velocity inhomogeneity and gives rise to a scattered wavefield. The scattered wavefield propagates upward to the surface where both the direct and scattered wavefields are recorded, see Figure 2.3. The scattered wavefield at position $\mathbf{x}$ due to a source at position $\mathbf{x_s}$ is denoted by $p_{sc}(\mathbf{x}, \mathbf{x_s}, t)$. It is the difference between the total recorded wavefield p and the background wavefield p_0:

$$p_{sc}(\mathbf{x}, \mathbf{x_s}, t) = p(\mathbf{x}, \mathbf{x_s}, t) - p_0(\mathbf{x}, \mathbf{x_s}, t). \tag{2.7}$$

The scattered wavefield can be approximated for any position $\mathbf{x}$ within a volume V enclosed by a surface S if the scattered wavefield and its normal derivative is known on S (Arntsen, 2019). The approximation can be computed by the surface integral given in equation (A.16) in Appendix A. Here, the notation $\hat{a}(t) = a(-t)$ is used. The sum $\Psi(\mathbf{x}, \mathbf{x_s}, t)$ is the sum of the anti causal scattered pressure $\hat{p}_{sc}$ for $t < 0$ and the causal scattered pressure p_{sc} for $t > 0$. The scattered wavefield at an arbitrary point $\mathbf{x}$ in V due to a source at $\mathbf{x_s}$, can be approximated by the following surface integral:

$$\begin{aligned}&\Psi(\mathbf{x}, \mathbf{x_s}, t) = p_{sc}(\mathbf{x}, \mathbf{x_s}, t) - \hat{p}_{sc}(\mathbf{x}, \mathbf{x_s}, t) = \\ &\int_S dS(\mathbf{x}')\rho^{-1}[\partial_{i'}\hat{p}_0(\mathbf{x}, \mathbf{x}', t) * p_{sc}(\mathbf{x}', \mathbf{x_s}, t) - \partial_{i'}p_{sc}(\mathbf{x}', \mathbf{x_s}, t) * \hat{p}_0(\mathbf{x}, \mathbf{x}', t)]n_i,\end{aligned} \tag{2.8}$$

where n_i is the surface normal on S in direction i, $i = (x, y, z)$ under Einstein's summation convention implying summation over repeated indices; $*$ is temporal convolution. It

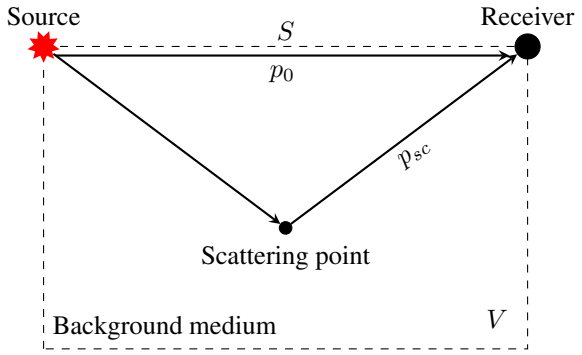

Figure 2.3: Illustration of the scattering problem. A wavefield induced by a source in a volume V propagates downwards to a scattering point. Here, it gives rise to a scattered wavefield that propagates towards the receiver. The total recorded wavefield p by a receiver on surface S is the sum of the direct wave p_0 and the scattered wavefield p_{sc}.

is assumed that the scattered wavefield $p_{sc}(\mathbf{x}', \mathbf{x_s}, t)$ due to a source at $\mathbf{x_s}$ and its normal derivative is known at position $\mathbf{x}'$ on S.

In true-amplitude angle gathers, the effect of geometrical spreading can be removed by moving both source and receiver to arbitrary positions at depth. Equation (2.8) gives the scattered wavefield at an arbitrary position $\mathbf{x}$ inside the volume V due to a source situated at position $\mathbf{x_s}$. As the source is normally situated close to the surface in a marine survey, the effect of geometrical spreading for the wave propagation from the source to the reflection point is not removed in Equation (2.8). The equation has to be modified so it gives the reflectivity where both the receiver and the source are positioned at arbitrary positions in depth to fully remove the effect of geometrical spreading.

Betti's reciprocal theorem states that the recorded seismic data is not affected by interchanging source and receiver locations (Ikelle, 2005). Source-receiver reciprocity for p_{sc} can be written as $p_{sc}(\mathbf{x}', \mathbf{x_s}, t) = p_{sc}(\mathbf{x_s}, \mathbf{x}', t)$. Applying this to equation (2.8) yields:

$$\Psi(\mathbf{x_s}, \mathbf{x}, t) = p_{sc}(\mathbf{x_s}, \mathbf{x}, t) * \hat{h}(t) - \hat{p}_{sc}(\mathbf{x_s}, \mathbf{x}, t) * h(t) = \int_S dS(\mathbf{x}')\rho^{-1}[\partial_{i'}\hat{p}_0(\mathbf{x}, \mathbf{x}', t) * p_{sc}(\mathbf{x_s}, \mathbf{x}', t) - \partial_i p_{sc}(\mathbf{x_s}, \mathbf{x}', t) * \hat{p}_0(\mathbf{x}, \mathbf{x}', t)]n_i. \tag{2.9}$$

Renaming $\mathbf{x_s}$ to $\mathbf{x}'$ and vice versa gives:

$$\Psi(\mathbf{x}', \mathbf{x_s}, t) = \int_S dS(\mathbf{x_s})\rho^{-1}[\partial_{i_s}\hat{p}_0(\mathbf{x}, \mathbf{x_s}, t) * p_{sc}(\mathbf{x}', \mathbf{x_s}, t) - \partial_{i_s} p_{sc}(\mathbf{x}', \mathbf{x_s}, t) * \hat{p}_0(\mathbf{x}, \mathbf{x_s}, t)]n_{i_s}. \tag{2.10}$$

After defining $r(\mathbf{x}', \mathbf{x}, t) = p_{sc}(\mathbf{x}, \mathbf{x_s}, t) * \hat{h}(t)$ and $\hat{r}(\mathbf{x}', \mathbf{x}, t) = \hat{p}_{sc}(\mathbf{x}, \mathbf{x_s}, t) * h(t)$,

equation (2.10) becomes:

$$r(\mathbf{x}', \mathbf{x}, t) - \hat{r}(\mathbf{x}', \mathbf{x}, t) = \int_S dS(\mathbf{x_s})\rho^{-1}[\partial_{z_s}\hat{p}_0(\mathbf{x}, \mathbf{x_s}, t) * \hat{p}_{sc}(\mathbf{x}', \mathbf{x_s}, t) - \partial_{z_s}p_{sc}(\mathbf{x}', \mathbf{x_s}, t) * \hat{p}_0(\mathbf{x}, \mathbf{x_s}, t)]. \tag{2.11}$$

The wavefield $r(\mathbf{x}', \mathbf{x}, t)$ given by equation (2.11) corresponds to a wavefield with virtual source and receiver positioned at arbitrary subsurface positions $\mathbf{x}$ and $\mathbf{x}'$, respectively. In other words, during reconstruction of the wavefield the sources and receivers are virtually moved from the surface to the subsurface and the effect of geometrical spreading is removed. True-amplitude angle gathers can therefore be constructed from this wavefield approximation. Measurements at the surface and an approximate pressure function p_0 are used to reconstruct $r(\mathbf{x}', \mathbf{x}, t)$. The migrated image is formed by moving the source and receiver to a scattering point and evaluating r by applying zero-lag temporal correlation. For an impulsive source, the zero-time lag correlation is nonzero at scattering points only.

As mentioned earlier, an accurate approximation of the background velocity model is required to obtain an accurate subsurface image. If the background model is inaccurate, the zero-lag temporal correlation will be nonzero near a scattering point, not at a scattering point. Likewise, applying wrong midpoint locations as a result of assuming nominal straight-line geometry will construct an image near a scattering point, not at a scattering point. This will show up as slightly defocused reflectors on the final migrated image due to traveltime erros, as shown in Section 2.1.4. Applying 3D migration with true source and receiver coordinates, this migration algorithm will cause the constructed wavefields to perfectly meet at the true subsurface location and true reflection coefficients can be estimated.

2.2.2 Imaging condition for single component streamer data

The surface integral in equation (2.11) is complex and both the pressure and its derivative have to be known in order to evaluate it. This can be simplified to (Thorbecke and Wapenaar, 2007):

$$r(\mathbf{x}', \mathbf{x}, t) - \hat{r}(\mathbf{x}', \mathbf{x}, t) = \int_S dS(\mathbf{x_s})\rho^{-1}\partial_{z_s}\hat{p}_0(\mathbf{x}, \mathbf{x_s}, t) * p_{sc}(\mathbf{x}', \mathbf{x_s}, t). \tag{2.12}$$

The resulting equation still leads to true amplitude-angle gathers. Evaluating equation (2.12) at $t = 0$ gives:

$$R(\mathbf{x}', \mathbf{x}) = r(\mathbf{x}', \mathbf{x}, t = 0) \approx 2\rho^{-1}\sum_{\mathbf{x_s}}\int dt\partial_{z_s}p_0(\mathbf{x}, \mathbf{x_s}, t)p_{sc}(\mathbf{x}', \mathbf{x_s}, t). \tag{2.13}$$

Further simplification can be done by neglecting the derivative and the density scaling in addition to placing the virtual sources and receivers at the same point $\mathbf{x}$:

$$R(\mathbf{x}) = r(\mathbf{x}' = \mathbf{x}, \mathbf{x}, t = 0) \approx \sum_{\mathbf{x_s}} \int dt p_0(\mathbf{x}, \mathbf{x_s}, t) p_{sc}(\mathbf{x}, \mathbf{x_s}, t) \tag{2.14}$$

This simplification leads to Claerbout's imaging condition (Claerbout, 1971) which does *not* lead to true-amplitude angle gathers. To achieve correct amplitude-versus-offset behavior, Equation (2.12) has to be applied.

2.2.3 Kirchhoff time migration-conventional approach

This section gives a numerical implementation of conventional time migration using Claerbout's approach given in Equation (2.14). The first step in time migration is to predict wavefield propagation. The wavefields involved in this approach are $p_0(x, x_s, t)$ and $p_{sc}(x, x_s, t)$.

The background pressure p_0 for a homogeneous medium can be described by $p_0(x, t) = g_0(x, t) * h(t)$. If $h(t) = \delta(t)$, then $p_0(x, t) = g_0(x, t)$. An approximate Green's function g_0 for a homogeneous medium is given by:

$$g_0(\mathbf{x}, \mathbf{x}', t) = \frac{\delta(t - r/c_0)}{r}, \tag{2.15}$$

where c_0 is the background p-wave velocity and r is given by:

$$r = r(\mathbf{x}, \mathbf{x}') = \mid \mathbf{x} - \mathbf{x}' \mid . \tag{2.16}$$

The following derivation follows a classical approach to time migration where scaling factors, derivatives and amplitudes are neglected. First, p_{sc} is computed for $t \geq 0$ by using equation (2.8):

$$p_{sc}(\mathbf{x}, \mathbf{x_s}, t) = \int_S dS(\mathbf{x}') \int d\tau \, p_{sc}(\mathbf{x}', \mathbf{x_s}, \tau) \frac{\delta(-t - \tau - r/c)}{r} \tag{2.17}$$

Integrating over τ gives:

$$p_{sc}(\mathbf{x}, \mathbf{x_s}, t) = \int_S dS(\mathbf{x}') \, p_{sc}(\mathbf{x}', \mathbf{x_s}, r/c + t) \tag{2.18}$$

The next step in migration is to apply an imaging condition to the predicted wavefields. Here, Claerbout's imaging condition as given in Equation (2.18) is used to relate p_0 and p_{sc} as given in Equations (2.15) and (2.18), respectively:

$$R(\mathbf{x}) = \int dS(\mathbf{x_s}) \int_S dS(\mathbf{x}') \int dt \frac{\delta(t - r/c)}{r} p_{sc}(\mathbf{x}', \mathbf{x_s}, r/c + t) \tag{2.19}$$

Evaluating the integral over t gives:

$$R(\mathbf{x}) = \int dS(\mathbf{x_s}) \int_S dS(\mathbf{x}') p_{sc}(\mathbf{x}', \mathbf{x_s}, 2r/c) \tag{2.20}$$

Inserting for r yields:

$$R(\mathbf{x}) = \int dS(\mathbf{x_s}) \int_S dS(\mathbf{x}') p_{sc} \left(\mathbf{x}', \mathbf{x_s}, t = \frac{2 \mid \mathbf{x} - \mathbf{x}' \mid}{c} \right). \tag{2.21}$$

The P-wave velocity c is normally estimated by a root-mean-square (RMS) zero-offset wave velocity v_{rms} given by

$$v_{rms}^2(t_0) = \frac{1}{t_0} \int_0^{t_0} v^2(t) dt, \tag{2.22}$$

where $v(t)$ is an interval velocity (Landrø, 2011). Inserting the RMS-velocity into Equation (2.21) gives:

$$R(\mathbf{x}) = \int dS(\mathbf{x_s}) \int_S dS(\mathbf{x}') p_{sc} \left(\mathbf{x}', \mathbf{x_s}, t = \frac{2 \mid \mathbf{x} - \mathbf{x}' \mid}{v_{rms}} \right). \tag{2.23}$$

Equation (2.23) is extremely simple and can be used to approximate the reflectivity at each subsurface point $\mathbf{x}$. For each trace, the traveltime from the source at $\mathbf{x_s}$ via the reflection point $\mathbf{x}$ to the true receiver position $\mathbf{x}'$ is calculated. Then, the amplitude found for the calculated traveltime at position $\mathbf{x}'$ is stored in a reflectivity map R. This is done for all possible traces. The result is a reflectivity map, or also known as a migrated image where the recorded energy has been relocated to its true subsurface location. The approach shown here is the conventional Kirchhoff time migration approach.

2.2.4 2D versus 3D imaging

The objective of 2D surveys is to generate a cross-section of the subsurface beneath the survey line. The recorded energy is assumed to be back-propagated from reflectors in the cross-section only. In reality, the recorded signal is the result of 3D wave propagation where out-of plane geological structures also contribute to the total recorded energy. A diffractor located out-of plane of the processing line will create reflections that back-propagate into the processing line. If 2D processing is applied, the recorded reflections will be imaged on the processing line, even though they do not belong to the processing plane, but rather out-of plane locations. Applying 3D migration to out-of plane reflections on a 2D section may help, but it requires crossline information, which is only available by recording data in 3D.

Imagine the cross-section at a point x perpendicular to the processing 2D section. A trace with traveltime t_0 located vertically below x can originate from any point on the semi-circle with radius z_0 and origin at x, as shown in Figure 2.4. An out-of plane reflection with traveltime t_0 is originally located somewhere on the semi-circle, and at a depth shallower than z_0. A reflection point situated outside the semi-circle and at a depth shallower than z_0 will have higher traveltime than t_0. It will appear on the seismic section below the reflection t_0, even though it is originally shallower. Both the depth of the out-of plane reflector and distance from the point x to the point vertically above the out-of plane reflector determine where out-of plane reflections will appear on a seismic section (Hobbs et al., 2006).

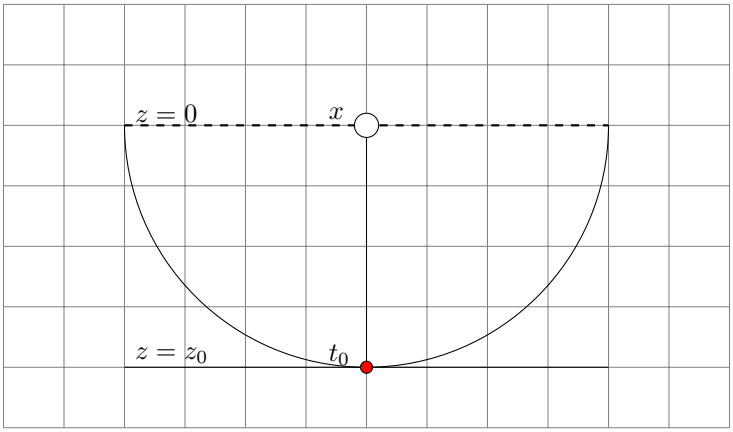

Figure 2.4: Illustration to explain traveltimes of out-of plane reflection. A signal with traveltime t_0 located vertically below a point x can belong to any place located on the semi-circle with radius z_0 and origin at x.

Migration focuses the energy on an unmigrated section by moving it to a point of diffraction. The energy in a 2D section is the same in an umigrated and migrated section, the only difference is the location of the energy. In the case of 3D migration, energy can be moved in and out of the different 2D sections of a 3D volume. Thus, the total energy in a section can increase or decrease during 3D migration, but is the same for the whole 3D volume before and after 3D migration. The energy from an out-of plane diffractor on a 2D section belongs to another 2D section. If 2D migration is applied, this energy will only be moved within the original 2D section, even though it does not belong there. 3D migration can move this energy to the 2D section it belongs to. Therefore, 2D migration and 3D migration can yield quite different results (Dondurur, 2018).

The energy from out-of plane reflections on data recorded in 2D can lead to mis-ties, smearing and an inaccurate, unfocused image (Biondi, 2006). Consider two perpendicular 2D sections, one in dip-direction and one in strike-direction. An out-of plane diffractor is recorded at the intersection between the two sections. The diffractor on the dip-line section will be migrated updip to its correct position. In strike-line direction, the same diffractor will not be moved as migration does not affect flat events. After migration, these two sections will mis-tie as the diffractor will be moved only for the dip-line section. During the process of migration, the recorded energy is first inserted into all locations it might have originated from. A strong amplitude will occur at the true reflection locations after all traces have been smeared out. The energy from out-of plane reflections will be left as smears on the migrated image as it does not belong to the 2D section and therefore cannot be relocated to its true location.

Chapter 3

Results

To investigate the effect of cable feathering on seismic data, synthetic data inspired by a seismic survey, *MY101*, with corresponding bathymetry data from the Japan Trench was used. A part of the survey is shown in Figure 3.1. Strong cross-currents caused the streamer to side-drift during the *MY101*-survey and turned the planned 2D survey into a limited swath 3D survey. The maximum streamer crossline offset was about $1000\,m$, while the mean offset was approximately $300\,m$. Wave propagation was simulated on a background model inspired by bathymetry data from the Japan Trench. The acquisition geometry was generated to simulate a feathered 2D survey, inspired by true coordinates from the *MY101* survey. Then, the synthetic data set was 2D and 3D migrated in order to investigate the possibility of diminishing the effect of feathering of 2D data by treating it as 3D data. A finite difference algorithm was used to solve the equations presented in Section 2.2. 3D migration of synthetic data based on the same background model, but with different acquisition geometries was also tested. The aim was to investigate how the resulting image was affected by various coverage.

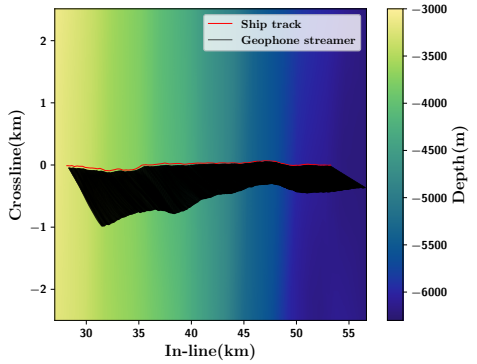

Figure 3.1: *MY101* survey.

This chapter presents the results of the synthetic tests. First, the background model and the different acquisition geometries are presented. Then, a presentation of the modeled data sets are given. Finally, the migrated images are compared. The 2D and 3D migrated images of feathered data are compared in order to see if treating the feathered 2D data as 3D data can improve the accuracy of the migrated image. Then, a comparison of the migrated images of the irregular and regular cases is made in order to see how the additional subsurface coverage affects the resulting image.

3.1 Background model

The background model presented here was used for both the simulated surveys. The model covered an area of $30\,km\,x\,5\,km\,x\,8\,km$, as shown in Figure 3.3. Real bathymetry data from the Japan Trench was used as inspiration during construction of the seafloor, see Figure 3.2. It had a gentle dip in in-line direction from approximately $3000\,m$ depth to $6300\,m$ depth. This gave an approximate dip of 7 degrees which yields an estimated depth difference of $3\,m$ for every $25th\,m$. Local depth variations were small enough to assume dip-independent stacking velocities. Therefore, the theory of stacking velocities for horizontal reflectors could be applied (Levin, 1971). A second, horizontal reflector was placed at $7250\,m$ depth. The wave velocities were set to $1500\,m/s$ for the water layer, $2200\,m/s$ for the first layer and $2300\,m/s$ for the second layer, see Figures 3.3a-3.3b. For simplicity, the density was assumed to be constant for the model. The background model was generated using a regular grid model with spatial sampling of $12.5\,m$ in all directions.

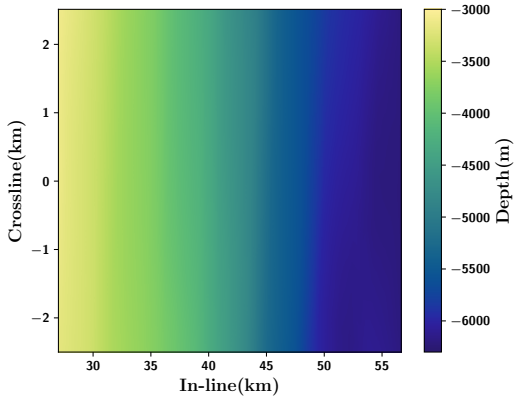

Figure 3.2: Bathymetry of velocity model.

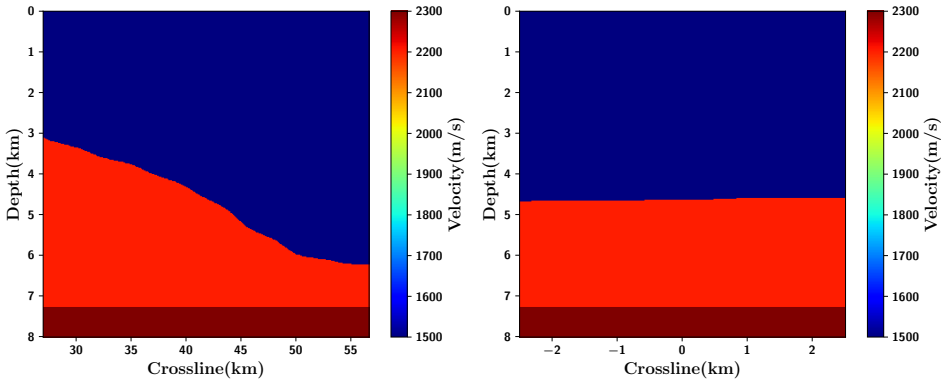

Figure 3.3: Velocity model (a) In-line direction (b) Crossline direction, at in-line position 42 km.

3.2 Acquisition geometries

Two different acquisition geometries were generated for the synthetic tests. A single streamer with receivers regularly spaced along the streamer at an interval of $25\,m$ was used for both surveys. The shotpoint interval was $50\,m$ for both surveys. A regular acquisition geometry was generated to represent a non-feathered 2D survey, as shown in Figure 3.4. Here, both the source and receiver crossline offsets were zero.

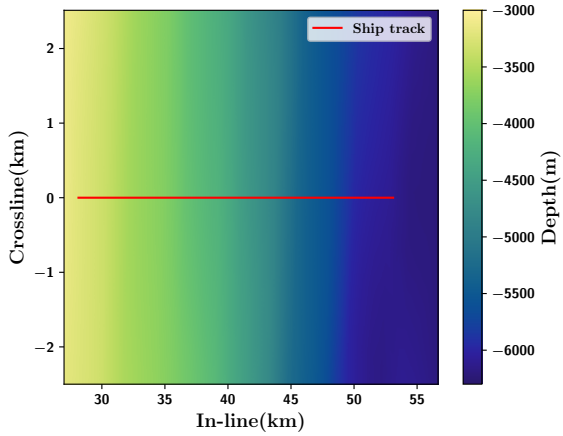

Figure 3.4: Regular/non-feathered acquisition geometry.

The second acquisition geometry is shown in Figure 3.5 and simulates a feathered survey. The streamer is shown for every $50th$ shotpoint. True source and receiver coordinates from the *MY101* survey were used to generate the feathered acquisition geometry. Figure 3.6 shows the streamer for the shotpoint with largest feathering. Here, the crossline error

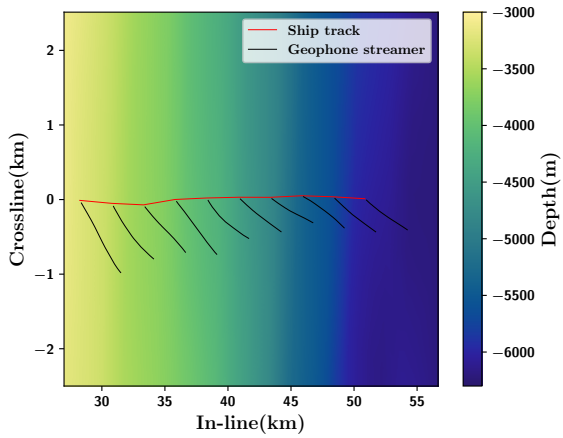

Figure 3.5: Irregular/feathered acquisition geometry.

reaches as high as $987\,m$. Overall, the streamer crossline feathering was approximately $300\,m$, as shown in Figure 3.7a. The source crossline error was much less, approximately $\pm 100\,m$ as shown in Figure 3.7b. For near-offsets, Figure 3.7c shows that the midpoint crossline error varied from $0\,m$ up to $125\,m$.

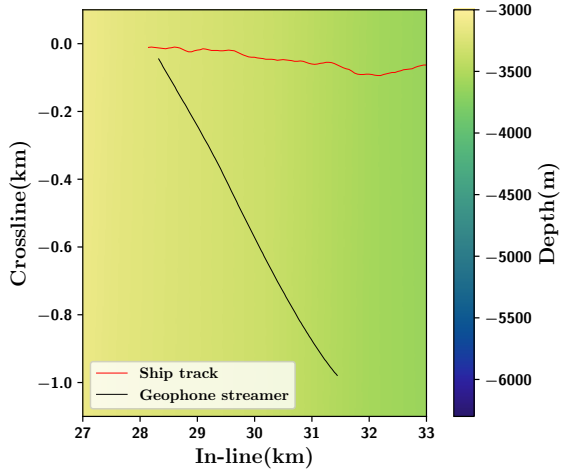

Figure 3.6: Shotpoint with largest streamer feathering.

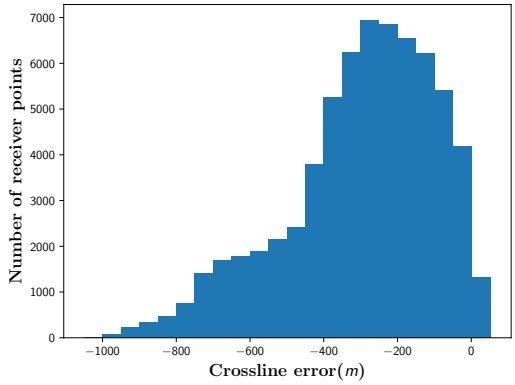

(a)

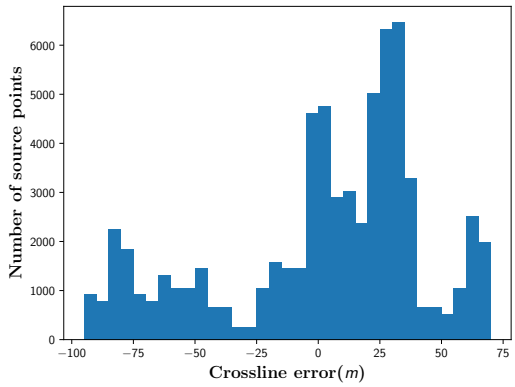

(b)

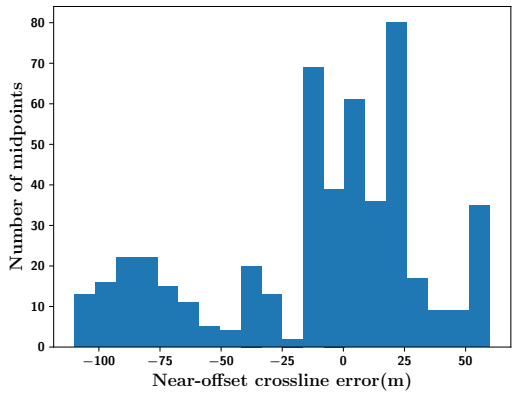

(c)

Figure 3.7: Crossline offset for (a) the receivers (b) the source (c) near-offset midpoints.

3.3 Modeling

A 3D acoustic wave equation modeling algorithm was used to simulate wave propagation based on the given background model with different acquisition setups. The simulated surveys were identical apart from source and receiver configurations. The surveys consisted of 522 shots. The source was situated at $10\,m$ depth and the streamer was situated at $15\,m$ depth. It held 132 active receivers spaced with $25\,m$ interval. The source pulse was created as a Ricker pulse with a peak frequency of $15\,Hz$ and time-lag of $0.1\,s$. The modeling aperture in crossline direction was set to $2500\,m$ as maximum feathering in crossline direction was $987\,m$. In in-line direction, the modeling aperture was set to $8000\,m$ as the streamer length was about $3300\,m$.

A time-domain finite difference scheme was used to solve the acoustic wave equation. In finite difference schemes, a finite system of linear equations are used to approximate the derivatives of the differential wave equation (LeVeque, 2007). Both time and space have to be discretized with a given time and spatial step. In order to avoid numerical instabilities in finite difference schemes, the sampling ratio between temporal sampling $\Delta\, t$ and spatial sampling $\Delta\, x$ has to be limited. It can be shown that the stability criteria for a second order scheme in three dimensions is given by (Landrø, 2011; Lines et al., 1999):

$$\frac{v_{p_{water}} \Delta t}{\Delta x} \leqq \frac{1}{\sqrt{3}}, \tag{3.1}$$

where Δx is the grid sampling, Δt is the temporal sampling and $v_{p_{water}}$ is the water velocity. In this case, $v_{p_{water}} = 1500\,m/s$, $\Delta x = 12.5\,m$ and $\Delta t = 4\,ms$ which satisfies Equation (3.1). The model parameters as given in Table 3.1. The modeling was implemented with a perfectly matching layer (PML) absorbing-boundary condition at the edges to avoid artefacts due to reflections from the grid edges. A free surface boundary at the surface was included as reflections from the sea surface is present in real experiments.

Seismic shot gathers as a result of modeling the irregular acquisition case is shown in Figure 3.8. Three different shots at different spatial locations are shown.

Grid parameters	
Spatial sampling (m)	12.5
Temporal sampling (ms)	4
In-line extent (km)	29
Crossline extent (km)	5
Depth (km)	8
Velocities	
Water velocity (m/s)	1500
Layer 1 velocity (m/s)	2200
Layer 2 velocity (m/s)	2300
Acquisition parameters	
Source depth (m)	10
Receiver depth (m)	15
Shotpoint interval (m)	50
Receiver interval (m)	25
Time sampling interval (ms)	4
Number of receiver channels	132
Number of shots	522
Modeling Parameters	
Source depth (m)	12.5
Receiver depth (m)	12.5
Ricker source frequency (Hz)	15
Source time-lag (s)	0.1
Crossline aperture (m)	2500
In-line aperture (m)	8000

Table 3.1: Model Parameters

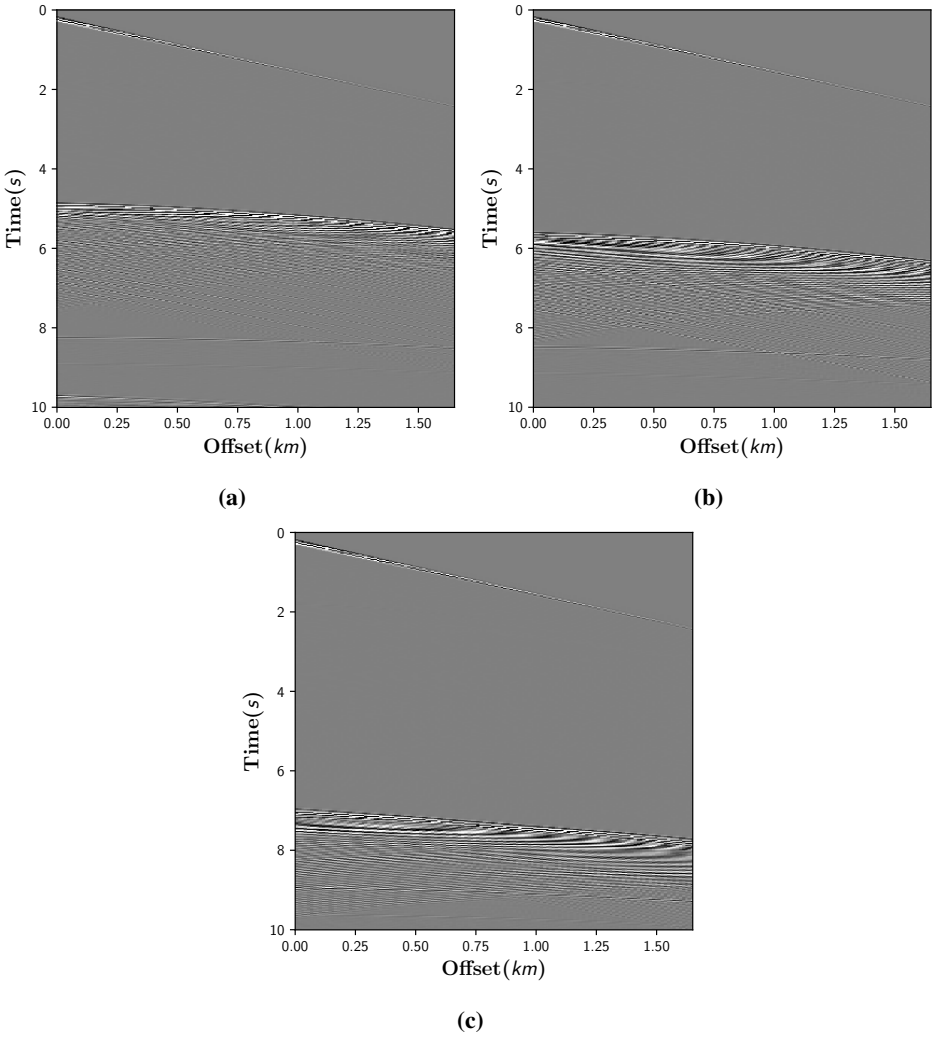

Figure 3.8: Shot gathers as a result of modeling with irregular acquisition geometry. (a) $\approx 3500m$ depth (b) $\approx 4500m$ depth (c) $\approx 5500m$ depth.

3.4 Migrated images

Prestack Kirchhoff time migration with antialising was applied to the modeled data sets. 3D migration was applied to the synthetic data sets generated by irregular and regular acquisition geometries. As the regular acquisition geometry has no crossline offset, applying 3D migration will basically be the same as applying 2D migration. In addition to 3D migration, the synthetic data generated from irregular acquisition geometry was also 2D migrated. 2D migration was applied by ignoring the crossline offset by setting the crossline coordinates to 0. No steps were taken to correct for the misplaced points. This was done in order to show the consequence of ignoring the 3D character of 2D feathered surveys by applying standard 2D processing methods without correcting for misplaced source and receivers.

Figure 3.9 shows the result of 3D migration of synthetic data generated from irregular acquisition geometry. The marked areas $1-4$ are zoomed in and compared for the tested methods. The dip of the reflector was not taken into account during migration therefore the migrated images may show some time-shift errors.

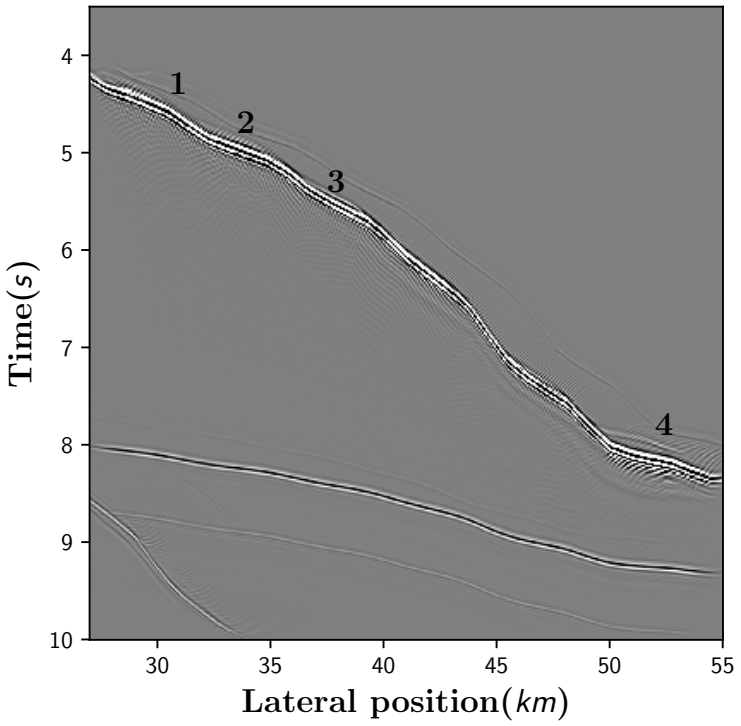

Figure 3.9: Migrated image generated from irregular single-streamer acquisition geometry.

3.4.1 2D and 3D migration of feathered synthetic data

Figures 3.11-3.12 show the 2D migrated images (left) and 3D migrated images (right) of the feathered synthetic survey. The 2D migrated images are overall less focused and the reflectors are much more smeared out compared to the 3D migrated images.

3D migration of the feathered data was applied without any corrections of the source and receiver coordinates. 2D migration of the feathered synthetic data was applied by assuming nominal straight-line geometry by setting all crossline offsets to zero without taking any steps to correct for the offset errors. Even with small crossline dip in the survey area, ignoring the crossline offset will result in traveltime errors. The zero-offset traveltime error, given by Equation (2.2), is computed from near-offset midpoints. From Figure 3.7c, the near-offset crossline error is generally less than $125\,m$. Figure 3.10 shows the depth difference $\pm\,125\,m$ from the nominal line relative to the depth at the nominal line. For most of the survey, the depth difference Δz is less than or equal to $10\,m$. The in-line near-offset midpoint error is small, and the depth difference for every $25th\,m$ is estimated to $3\,m$. It is fair to assume an overall maximum depth difference due to midpoint error to be $13\,m$. For a stacking velocity of $1500\,m/s$, Equation (2.2) gives a maximum zero-offset traveltime error Δt_0 of $17\,ms$ as a result of assuming straight-line geometry for the feathered data.

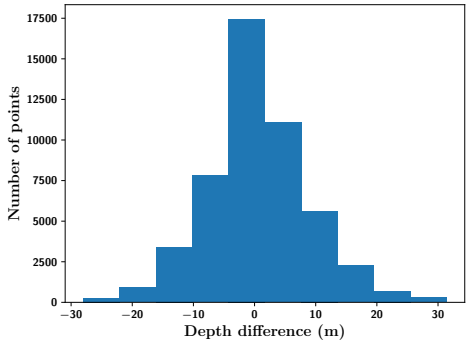

Figure 3.10: Depth differences $\pm 125\,m$ from the nominal line. Depth differences are relative to the depth of the nominal line.

The largest crossline offset is $987\,m$ and occurs at lateral position $31.4\,km$, see Figure 3.6. The source-receiver offset x is 3269 m and assuming straight-line geometry gives an offset error Δx of 146 m. For a traveltime t of $4.5\,s$, the traveltime error Δt, given by Equation (2.3), is estimated to $\approx 65\,ms$ for the largest crossline offset.

The 3D migrated image in Figure 3.11b shows a much more focused image of the area with largest crossline error compared to the 2D migrated image in Figure 3.11a. The crossline offset is not this high for the rest of the survey line, but generally about $300\,m$. This leads to a traveltime error less than $65\,ms$, but still large enough to result in distorted images. The 3D migrated images in Figures 3.11b-3.12d are in general much more focused than the corresponding 2D migrated images, as can be expected due to the traveltime errors. The 3D migrated image in Figure 3.12d is less focused than the corresponding

2D migrated image. At that location, crossline depth differences are the highest and most variable compared to the rest of the survey area.

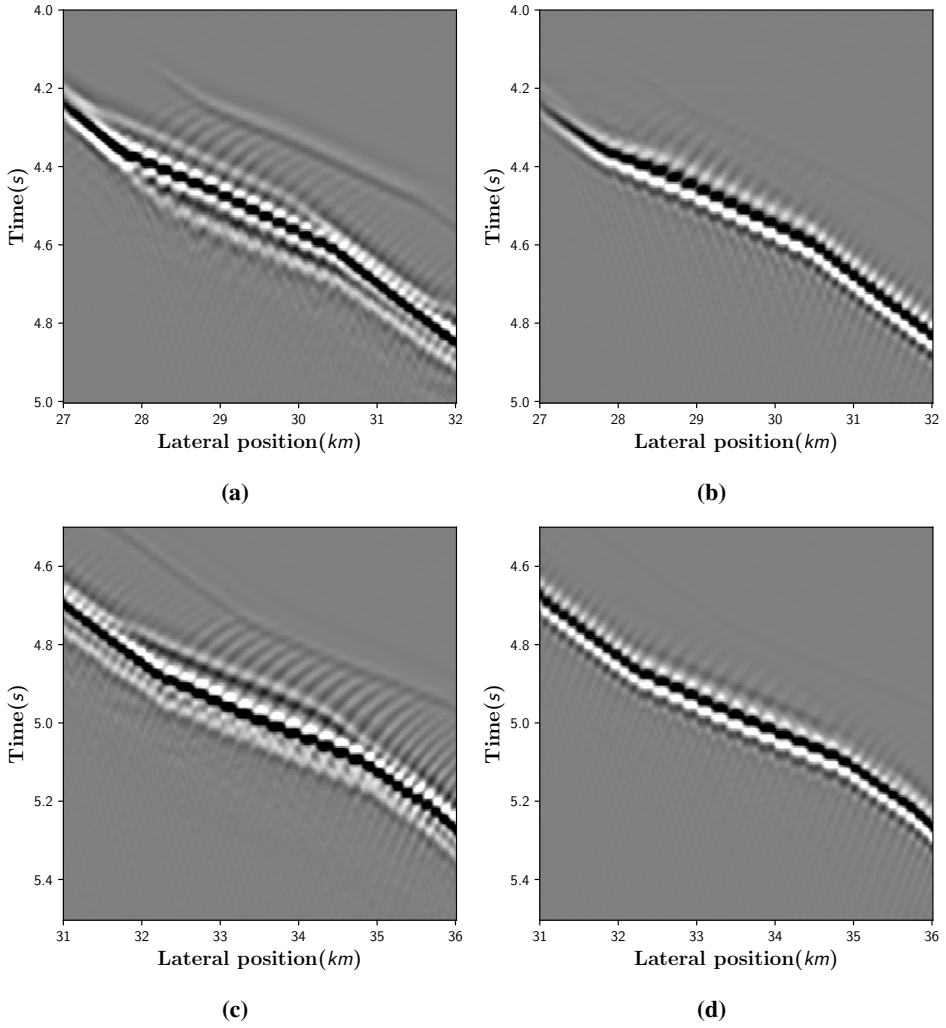

Figure 3.11: Migrated images of data generated from irregular single-streamer acquisition geometry of position 1 (a,b) and position 2 (c,d) by (a,c) 2D migration and (b,d) 3D migration.

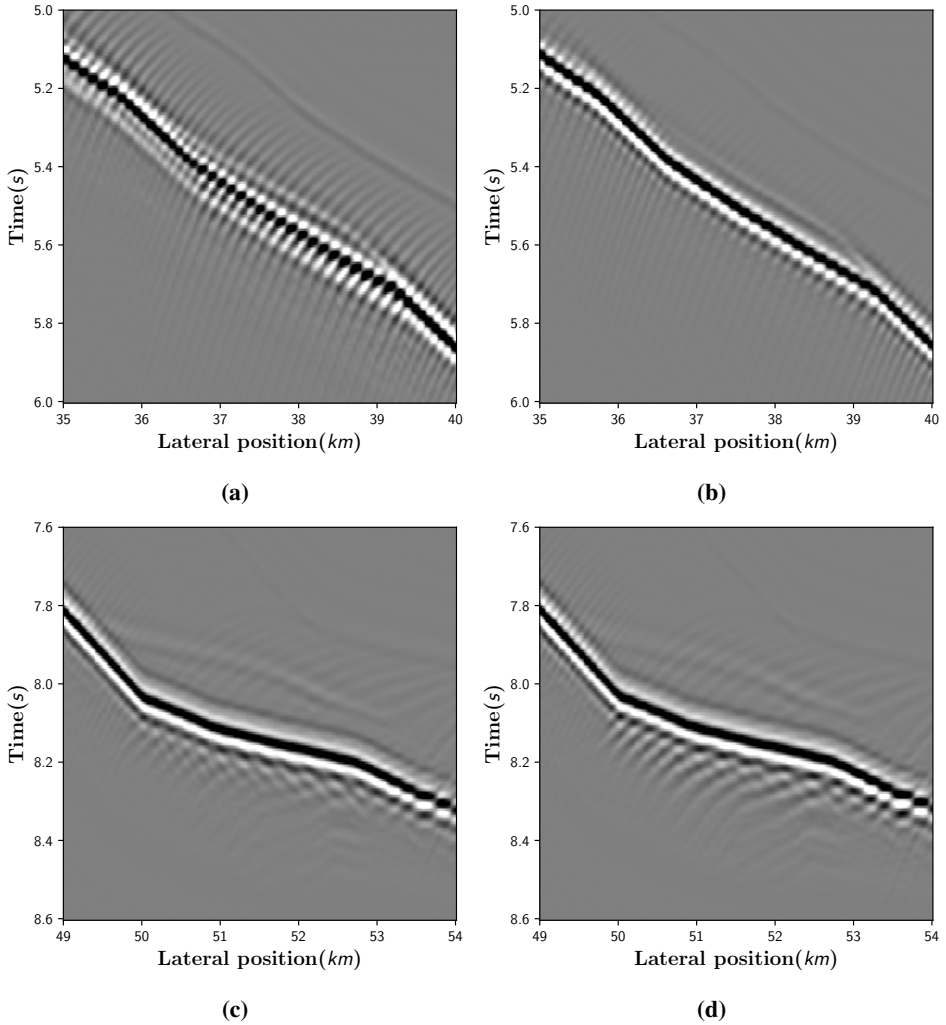

Figure 3.12: Migrated images of data generated from irregular single-streamer acquisition geometry of position 3 (a,b) and position 4 (c,d) by (a,c) 2D migration and (b,d) 3D migration.

3.4.2 3D migration of feathered and non-feathered synthetic data

3D migration of the synthetic data generated from regular and irregular acquisition geometries are shown in Figures 3.13-3.14. The right side shows the feathered case and the left side shows the regular case. As mentioned above, 3D migration of the regular case was basically the same as 2D migration since the survey is in fact a 2D survey.

Unlike the nominal feathered case, the regular case did not cause traveltime errors due to midpoint errors. Instead, traveltime errors occur due to out-of plane reflections. Data collected in a 2D survey is assumed to originate from 2D structures in the vertical cross-section below the survey line. Actually, out-of plane reflectors and diffractors also contribute to the recorded data. Even with 3D migration, the recorded data does not provide enough information to migrate the recorded energy back to its origin. 2D migration will only migrate the recorded energy within the 2D section. The energy reflected from out-of plane reflectors will be migrated within the actual 2D section, even though it does not belong there. The energy will be moved to places it might have originated from within the 2D section and therefore cause crossline smearing.

In the previous example, a maximum depth difference Δz due to midpoint error was estimated to $13\,m$. Using the same estimation, the maximum depth difference $\pm\,125\,m$ from the processing line is $13\,m$. Figure 3.10 shows that the depth relative to depth at the nominal line is variable in crossline direction. An out-of plane reflection can therefore appear on the zero-offset section at the same time as an in-plane reflection with equal traveltime. Originally, the out-of plane reflection will be shallower than the in-plane reflection. 2D migration will migrate the out-of plane reflection to an in-plane location deeper than the true location. This can cause smearing artifacts on the migrated image.

The feathered streamer collected data in 3D which made it possible to migrate energy back to out-of plane locations. The 3D geometry of the acquired data held information that made it possible to estimate where the energy belonged. Bettis theorem of cross-correlation was used to back-propagate out-of plane reflections to their original location by relating wavefields recorded at different locations. The migrated images in Figures 3.11-3.12 are less focused and much more distorted for the 2D migrated case than the 3D migrated case. Crossline depth variations at $45\,km$ to $54\,km$ reached up to $30\,m$ and were much more variable at that area than for the rest of the line. Therefore, out-of plane contributions were higher at this location which caused more smearing of the reflectors for the regular case than the feathered case, as can be seen in Figures 3.14c-3.14d.

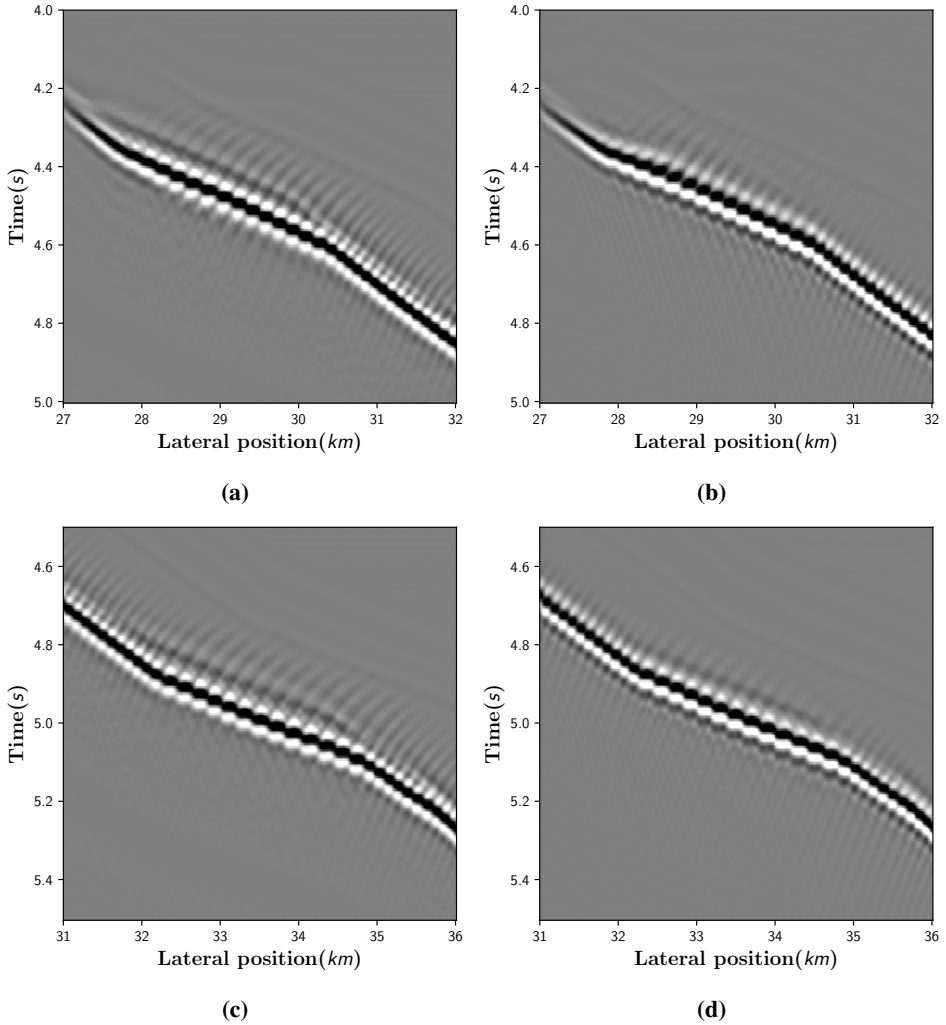

Figure 3.13: 3D migrated images of position 1 (a,b) and position 2 (c,d) generated from (a,c) regular acquisition geometry (b,d) irregular acquisition geometry.

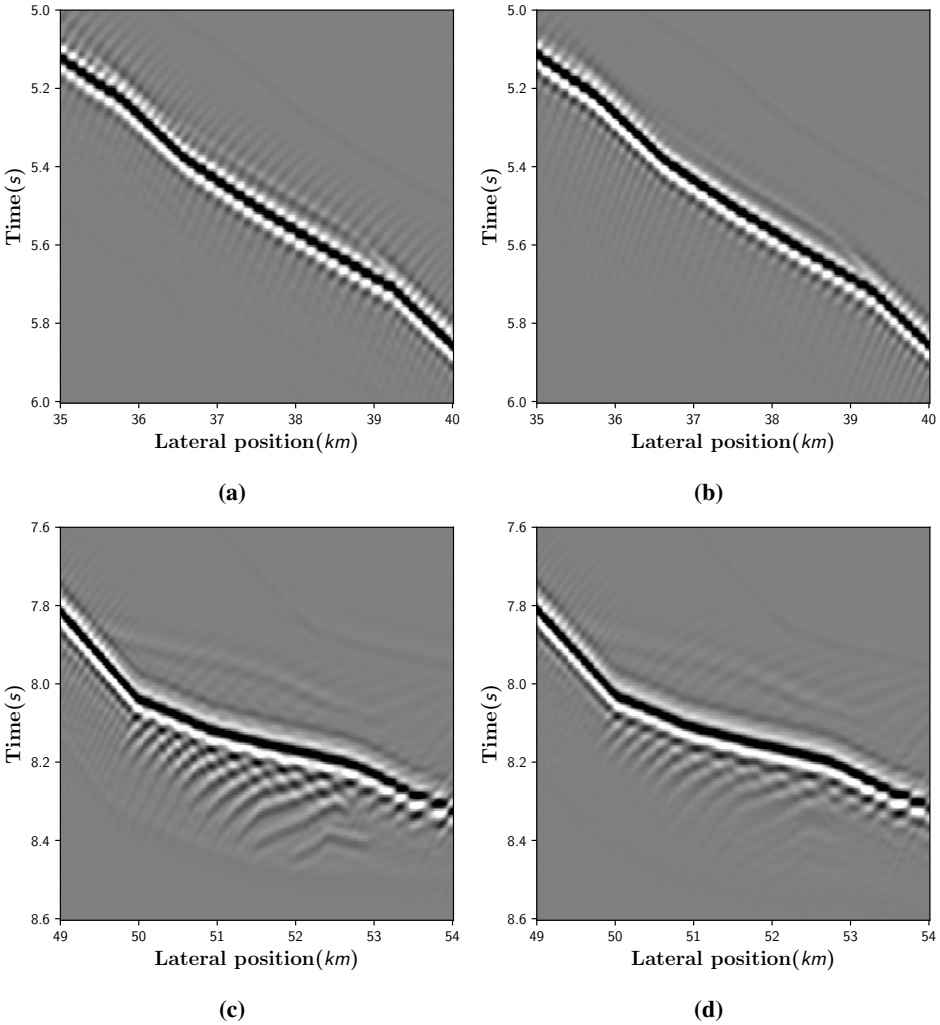

Figure 3.14: 3D migrated images of position 3 (a,b) and position 4 (c,d) generated from (a,c) regular acquisition geometry and (b,d) irregular acquisition geometry.

Chapter 4

Discussion

The objective of seismic migration is to render an accurate image of subsurface geologic structures. This is done by focusing the recorded energy at its true subsurface location. In migration by wave theory, the recorded data is back propagated into the subsurface while a synthetic source wavefield is forward propagated into the subsurface. An imaging condition is used to correlate these wavefields and create an image where the two wavefields coincide. A true amplitude cross-correlation imaging condition was developed in Section 2.2. It is able to estimate wavefields with virtual subsurface source and receiver from measurements at the surface. This removes the effect of geometrical spreading and produces correct reflectivity based on angle-dependency.

An accurate image is achieved if the recorded energy is migrated back to its original location. This requires the knowledge of true source and receiver locations. Assuming 2D nominal geometry for a feathered 2D survey without taking steps to correct for the offset error migrates the recorded energy to a location in near vicinity of its true location. The result is an unfocused migrated image, as can be seen in Figures 3.11a-3.12c.

By treating the feathered 2D data as 3D data, true source and receiver coordinates are used to back propagate the recorded energy to its true location. Even with an irregular midpoint distribution and a limited offset range, the 3D migrated images in Figures 3.11b-3.12d show improved imaging accuracy compared to the 2D migrated images. For the shallow traveltimes where the depth differences relative to the nominal line is small, 3D migration method gives a more accurate image than the nominal 2D migration method. For deeper depths where the depth difference varies more, 3D migration fails to improve imaging. Limited offset range combined with complex subsurface geometry can explain why the method fails for the deeper depths. In 3D migration, energy can be moved between 2D sections that make up a 3D volume. The total energy of a 2D section can therefore increase or decrease during the process. 3D migration gives a large amount of possible true reflection points as energy can be moved in and out of the 2D sections. 2D migration only moves energy within the only available 2D section. This can explain why the nominal migrated feathered case gives a better result than the 3D migrated feathered case. Smearing of data is more pronounced for the 3D migrated feathered case as the total number of

possible reflection points is greater. In addition, traveltime errors due to offset errors will be smaller for larger traveltimes.

Assuming nominal straight-line geometry is a very simple approach in dealing with misplaced midpoints due to feathered streamers. Time-lapse seismic has become an important seismic tool during the last decades. A high repeatability between surveys is required to monitor subtle subsurface changes and sophisticated interpolation schemes has therefore been developed to account for low repeatability between surveys. In a time-lapse study using seismic data acquired before and after the Tohoku-Oki earthquake in 2011, Landrø et al. (2019) used an interpolation scheme based on Shepard's algorithm (Shepard, 1968) to ensure higher repeatability between the surveys. Our tests are inspired by the baseline survey acquired in 1999, the *MY101* survey. Both the baseline and monitor surveys were feathered by strong cross currents. The interpolation scheme increased the repeatability between the surveys enough to enable a study of the time-lapse effects. A test to investigate the errors due to feathering after corrections were made shows that it yields a minimal impact. We propose a study to compare our approach of treating feathered 2D data as 3D data to an approach similar to Landrø's approach of interpolating the feathered data onto a 2D line.

Out-of plane reflections are recorded in both 2D and 3D surveys, but only data recorded by 3D surveys provide enough information to correctly migrate the out-of plane reflections. 3D migration of data collected along a nominal line is not able to back propagate out-of plane energy to the true location, no matter how sophisticated the method is. Betti's reciprocity theorem of the cross-correlation type was used to develop the novel imaging condition in Section 2.2.1. The theorem correlates a wavefield in two different media. The true location of out-of plane reflections are predicted by correlating the wavefield recorded by several receivers. To do this, recordings acquired at an angle to the processing line is required. The 3D migrated images of the feathered 2D survey shows a significantly higher accuracy than the 2D migrated images of the regular survey. For the area with most variable crossline depths, 3D migration gives a remarkably better result. Instead of trying to correct for errors due to feathering, treating the data as 3D data increases the imaging accuracy and turns feathering to an advantage.

Nedimović et al. (2003) also took advantage of the additional information available as a result of feathering. Crossline dip information was extracted from the feathered data by an optimum cross-dip stack procedure. Both 2D and 3D post-stack migration was applied to the optimum cross-dip stack. The method shows good results for areas of moderate dip and small lateral velocity variations, but fails to improve imaging of the complex areas. Nedimović suggest 3D prestack migration of feathered 2D data in areas with very complex subsurface geology to further improve imaging of complex areas.

It is necessary to emphasize that the background model used in our examples is simple with a gentle in-line dip and small crossline variations. As Nedimović suggests, the method should be tested on a complex model, preferably with a steeper in-line dip and geologic 3D structures in crossline direction. We also suggest a study to compare 3D migration of a feathered single-streamer survey and feathered multistreamer surveys. We are curious to see the impact the additional coverage has on the migrated images.

Chapter 5

Conclusion

Studying the effect streamer feathering has on seismic 2D data shows clear evidence of a 3D dependency of the feathered data. When we apply nominal straight-line geometry to feathered data followed by 2D processing methods, traveltime errors due to misplaced source and receiver positions leads to unfocused reflectors and crossline smearing. When we take into account the 3D character of the feathered data by applying 3D migration, we avoid the same traveltime errors due to midpoint errors that occur when 2D processing methods are applied. 3D migration is able to handle irregularly sampled data and true source and receiver coordinates can be used. The result is improved imaging accuracy compared to applying nominal straight-line geometry. The novel imaging condition presented in Section 2.2.1 support our results. By relating the simulated source and receiver wavefield for each time step, an image is constructed where they coincide. When wrong coordinates are applied, the wavefields coincide in near vicinity of the true location. On the migrated sections, this is seen as a slight defocusing of the reflectors. This fits with our observations. The 3D migrated images of the feathered data show increased focusing and less crossline smearing compared to the 2D migrated images of the feathered data.

Furthermore, we have shown that streamer feathering can be an advantage if handled correctly. We observe that the extra information provided by streamer feathering yields increased imaging accuracy compared to regular 2D data when taken into account. Seismic data recorded in 2D is not able to adequately migrate out-of plane reflections as it requires unavailable 3D information. Streamer feathering can provide the required 3D information which enables correct migration of out-of plane reflections, at least in areas with simple subsurface geology.

Our experiments show good results based on a simple reflection model. Imaging of complex subsurface structures may require more information than a limited swath 3D survey provides. We recommend further tests on a complex model, preferably with 3D geologic structures in crossline direction. The effect of feathering on multistreamer data has not been studied. It would be interesting to see if the additional coverage gives improved imaging accuracy compared to a feathered single-streamer survey.

We have shown that 2D seismic feathered data has to be processed as 3D data to

achieve improved imaging accuracy. Our approach is to apply 3D migration without any corrections. So far, it has shown promising results. Another approach is to apply advanced 3D interpolation schemes followed by 2D processing methods (Landrø et al., 2019). We propose a study to see which approach gives increased imaging accuracy.

Bibliography

Arntsen, B., 2019. True amplitude cross-correlation imaging condition for reverse time migration.

Biondi, B. L., 2006. 3D seismic imaging. Society of Exploration Geophysicists, Tulsa, Oklahoma.

Claerbout, J. F., 1971. Toward a unified theory of reflector mapping. Geophysics 36 (3), 467–481.

Cooper, M., Westwater, P., Thorogood, E., Kristiansen, P., Christie, P., 1999. Foinaven active reservoir management; towed streamer and buried seabed detectors in deep water for 4-d seismic. Vol. 69. Society of Exploration Geophysicists, Tulsa, Oklahoma, pp. 1632–1635.

Dondurur, D., 2018. Acquisition and Processing of Marine Seismic Data. Elsevier Science.

Eiken, O., Haugen, G. U., Schonewille, M., Duijndam, A., 2003. A proven method for acquiring highly repeatable towed streamer seismic data. Geophysics 68 (4), 1303–1309.

Goto, R., Lowden, D., Smith, P., Paulsen, J. O., Osdal, B., Aronsen, H., 2004. Steered-streamer 4d case study over the norne field. SEG Technical Program Expanded Abstracts 23 (1), 2227–2230.

Gulick, S. P. S., Bangs, N. L. B., Shipley, T. H., Nakamura, Y., Moore, G. F., Kuramoto, S., 2004. Three dimensional architecture of the nankai accretionary prism's imbricate thrust zone off cape muroto, japan: Prism reconstruction via en echelon thrust propagation. Journal of Geophysical Research: Solid Earth 109 (B2).

Hobbs, R., Drummond, B., Goleby, B., 2006. The effects of three-dimensional structure on two-dimensional images of crustal seismic sections and on the interpretation of shear zone morphology. Geophysical Journal International 164 (3).

Ikelle, L. T., 2005. Introduction to petroleum seismology.

Kalra, A. K., 1986. Velocity analysis for feathered marine data. Geophysics 51 (1), 190–191.

Krail, P. M., Brysk, H., 1989. The shape of a marine streamer in a cross current. Geophysics 54 (3), 302–308.

Landrø, M., 2011. Seismic data acquisition and imaging.

Landrø, M., Kodaira, S., Fujiwara, T., No, T., Weibull, W. W., Arntsen, B., 2019. Time lapse seismic analysis of the tohoku-oki 2011 earthquake.
URL http://hdl.handle.net/11250/2581594

LeVeque, R. J., 2007. Finite difference methods for ordinary and partial differential equations: steady-state and time-dependent problems.

Levin, F. K., 1971. Apparent velocity from dipping interface reflections. Geophysics 36 (3), 510–516.

Levin, F. K., 1983. The effects of streamer feathering on stacking. Geophysics 48 (9), 1165–1171.

Levin, F. K., 1984. The effect of binning on data from a feathered streamer. Geophysics 49 (8), 1386–1387.

Lines, L., Slawinski, R., Bording, R., 1999. A recipe for stability of finite-difference wave-equation computations. Geophysics 64 (3), 967–969.

Nedimović, M. R., Mazzotti, S., Hyndman, R. D., 2003. Three-dimensional structure from feathered two-dimensional marine seismic reflection data: The eastern nankai trough. Journal of Geophysical Research: Solid Earth 108 (B10).

Shepard, D., 1968. A two-dimensional interpolation function for irregularly-spaced data. In: Proceedings of the 1968 23rd ACM National Conference, ACM 1968. Association for Computing Machinery, Inc, pp. 517–524.

Thorbecke, J., Wapenaar, K., 2007. On the relation between seismic interferometry and the migration resolution function. Geophysics 72 (6), T61–T66.

van Borselen, R. G., Fokkema, J., van den Berg, P., 2013. Wavefield decomposition based on acoustic reciprocity; theory and applications to marine acquisition. Geophysics 78 (2), WA41–WA54.

Vesnaver, A. L., Accaino, F., Bohm, G., Madrussani, G., Pajchel, J., Rossi, G., Dal Moro, G., 2003. Time-lapse tomography. Geophysics 68 (3), 815–823.

Zwartjes, P., Gisolf, A., 2006. Fourier reconstruction of marine streamer data in four spatial coordinates. Geophysics 71 (6), V171–V186.

Appendix

A Scattering integral

For an acoustic medium characterized by density ρ and bulk modulus κ, wavefield propagation can be described by the equation of motion (A.1) and the constitutive relation (A.2) given by:

$$\rho(\mathbf{x})\partial_t^2 u_i(\mathbf{x},t) = \partial_i p(\mathbf{x},t), \tag{A.1}$$

$$p(\mathbf{x},t) = \kappa(\mathbf{x})\partial_i u_i(\mathbf{x},t) + q(\mathbf{x},t), \tag{A.2}$$

where $\mathbf{x} = (x, y, z)$ is the spatial position; t is the time; u_i is the particle displacement in direction i; p is the acoustic pressure; q is a source of injection type and $i = (x, y, z)$. The notation ∂_i denotes the spatial derivative in direction i.

For another acoustic medium characterized by density ρ_0 and bulk modulus κ_0, the particle displacement u_0 and pressure p_0 satisfy the same equation of motion and the same constitutive relation as above:

$$\rho_0(\mathbf{x})\partial_t^2 u_{0i}(\mathbf{x},t) = \partial_i p_0(\mathbf{x},t), \tag{A.3}$$

$$p_0(\mathbf{x},t) = \kappa_0(\mathbf{x})\partial_i u_{0i}(\mathbf{x},t) + q_0(\mathbf{x},t), \tag{A.4}$$

where q_0 is a source of injection type.

Consider a volume V in space enclosed by a surface S with surface normal n directed away from V. The two cases of acoustic wavefield propagation described by Equations (A.1)-(A.4) can both occur in volume V. Betti's reciprocal theorem of the cross-correlation type can be used to relate the wavefield in the two acoustic media (van Borselen et al., 2013; Ikelle, 2005).

Here, the pressure $p = p(x, x_s, t)$ at position x due to a source at position x_s can be related to the pressure $p_0 = p_0(x, x'_s, t)$ at position x due to a source at position x'_s. Considering the anticausal state of the wavefield p denoted by $\hat{p}$, where $\hat{a}(t) = a(-t)$, applying the reciprocity theorem to equations (A.1)-(A.4) gives:

$$\begin{aligned}\int_V dV(\partial_t^2 q_0 * \hat{p} - \partial_t^2 \hat{q} * p_0) = \int_S dS[\rho_0^{-1}\partial_i p_0 * \hat{p} - \rho^{-1}\partial_i \hat{p} * p_0]n_i + \\ \int_V dV(\lambda - \lambda_0)\partial_t p_0 * \partial_t \hat{p} + \int_V dV \frac{(\rho - \rho_0)}{\rho\rho_0}\partial_i p_{0i} * \partial_i \hat{p}_i,\end{aligned} \tag{A.5}$$

where $\lambda = \kappa^{-1}$; $\lambda_0 = \kappa_0^{-1}$ and $*$ denotes time convolution, defined by:

$$a(t) * b(t) = \int_0^t d\tau\, a(t-\tau)b(\tau), \tag{A.6}$$

where a and b are arbitrary functions. The seismic source q_0 is a source of injection type at point $\mathbf{x}'_\mathbf{s}$ with impulse response function $h(t)$ such that $\partial_t^2 q_0(\mathbf{x},t) = \delta(\mathbf{x} - \mathbf{x}'_\mathbf{s})h(t)$. Here, δ is Dirac's delta function and the sifting property of the Dirac delta function is given by:

$$\int dx f(x)\delta(x-a) = f(a), \tag{A.7}$$

where f is an arbitrary function. The seismic source q is a seismic source of injection type at point $\mathbf{x_s}$ and source pulse $\mathbf{s(t)}$ such that $\partial_t^2 \hat{q}(\mathbf{x}, t) = \delta(\mathbf{x} - \mathbf{x_s})\hat{s}(t)$. Substituting into Equation (A.5) and applying the sifting property of the Dirac delta function gives:

$$\hat{p}(\mathbf{x'_s}, \mathbf{x_s}, t) * h(t) - p_0(\mathbf{x_s}, \mathbf{x'_s}, t) * \hat{s}(t) =$$
$$\int_S dS(\mathbf{x})[\rho_0^{-1}\partial_i p_0(\mathbf{x}, \mathbf{x'_s}, t) * \hat{p}(\mathbf{x}, \mathbf{x_s}, t) - \rho^{-1}\partial_i \hat{p}(\mathbf{x}, \mathbf{x_s}, t) * p_0(\mathbf{x}, \mathbf{x'_s}, t)]n_i +$$
$$\int_V dV(\mathbf{x})(\lambda - \lambda_0)\partial_t p_0(\mathbf{x}, \mathbf{x'_s}, t) * \partial_t \hat{p}(\mathbf{x}, \mathbf{x_s}, t) + \int_V dV \frac{(\rho - \rho_0)}{\rho\rho_0}\partial_i p_{0i}(\mathbf{x}, \mathbf{x'_s}, t) * \partial_i \hat{p}_i(\mathbf{x}, \mathbf{x_s}, t). \tag{A.8}$$

If the medium parameters are identical for the two acoustic states, i.e. $\lambda_0 = \lambda$ and $\rho_0 = \rho$, the pressure $\hat{p}_0$ can be determined from Equation (A.8):

$$\hat{p}_0(\mathbf{x'_s}, \mathbf{x_s}, t) * h(t) - p_0(\mathbf{x_s}, \mathbf{x'_s}, t) * \hat{s}(t) =$$
$$\int_S dS(\mathbf{x})\rho_0^{-1}[\partial_i p_0(\mathbf{x}, \mathbf{x'_s}, t) * \hat{p}_0(\mathbf{x}, \mathbf{x_s}, t) - \partial_i \hat{p}_0(\mathbf{x}, \mathbf{x_s}, t) * p_0(\mathbf{x}, \mathbf{x'_s}, t)]n_i. \tag{A.9}$$

The anticausal scattered wavefield $\hat{p}_{sc}$ is defined by $\hat{p}_{sc} = \hat{p} - \hat{p}_0$. Subtracting equation (A.9) from equation (A.8) gives the anticausal scattered wavefield :

$$\hat{p}_{sc}(\mathbf{x'_s}, \mathbf{x_s}, t) * h(t) =$$
$$\int_S dS(\mathbf{x})\rho^{-1}[\partial_i p_0(\mathbf{x}, \mathbf{x'_s}, t) * \hat{p}_{sc}(\mathbf{x}, \mathbf{x_s}, t) - \partial_i \hat{p}_{sc}(\mathbf{x}, \mathbf{x_s}, t) * p_0(\mathbf{x}, \mathbf{x'_s}, t)]n_i +$$
$$\int_V dV[(\lambda - \lambda_0)\partial_t \hat{p}(\mathbf{x}, \mathbf{x_s}, t) * \partial_t p_0(\mathbf{x}, \mathbf{x_s}, t) + \frac{(\rho - \rho_0)}{\rho\rho_0}\partial_i \hat{p}_i(\mathbf{x}, \mathbf{x_s}, t) * \partial_i p_{0i}(\mathbf{x}, \mathbf{x'_s}, t)]. \tag{A.10}$$

Here, it is assumed that ρ and ρ_0 are equal at the boundary S. The reciprocity theorem also states that the recorded seismic trace is not affected when the source and receiver are interchanged (Ikelle, 2005). Interchanging source and receiver for p_0, that is $p_0(x, x'_s, t) = p_0(x'_s, x, t)$, yields:

$$\hat{p}_{sc}(\mathbf{x'_s}, \mathbf{x_s}, t) * h(t) =$$
$$\int_S dS(\mathbf{x})\rho^{-1}[\partial_i p_0(\mathbf{x'_s}, \mathbf{x}, t) * \hat{p}_{sc}(\mathbf{x}, \mathbf{x_s}, t) - \partial_i \hat{p}_{sc}(\mathbf{x}, \mathbf{x_s}, t) * p_0(\mathbf{x'_s}, \mathbf{x}, t)]n_i +$$
$$\int_V dV[(\lambda - \lambda_0)\partial_t \hat{p}(\mathbf{x}, \mathbf{x_s}, t) * \partial_t p_0(\mathbf{x'_s}, \mathbf{x}, t) + \frac{(\rho - \rho_0)}{\rho\rho_0}\partial_i \hat{p}_i(\mathbf{x}, \mathbf{x_s}, t) * \partial_i p_{0i}(\mathbf{x'_s}, \mathbf{x}, t)]. \tag{A.11}$$

Renaming $\mathbf{x}$ to $\mathbf{x'}$ gives:

$$\hat{p}_{sc}(\mathbf{x'_s}, \mathbf{x_s}, t) * h(t) =$$
$$\int_S dS(\mathbf{x'})\rho^{-1}[\partial_{i'} p_0(\mathbf{x'_s}, \mathbf{x'}, t) * \hat{p}_{sc}(\mathbf{x'}, \mathbf{x_s}, t) - \partial_{i'} \hat{p}_{sc}(\mathbf{x'}, \mathbf{x_s}, t) * p_0(\mathbf{x'_s}, \mathbf{x'}, t)]n_i +$$
$$\int_V dV[(\lambda - \lambda_0)\partial_t \hat{p}(\mathbf{x'}, \mathbf{x_s}, t) * \partial_t p_0(\mathbf{x'_s}, \mathbf{x'}, t) + \frac{(\rho - \rho_0)}{\rho\rho_0}\partial_{i'} \hat{p}_i(\mathbf{x'}, \mathbf{x_s}, t) * \partial_{i'} p_{0i}(\mathbf{x'_s}, \mathbf{x'}, t)]. \tag{A.12}$$

Further renaming $\mathbf{x}'_\mathbf{s}$ to $\mathbf{x}$:

$$\hat{p}_{sc}(\mathbf{x}, \mathbf{x_s}, t) * h(t) =$$
$$\int_S dS(\mathbf{x}')\rho^{-1}[\partial_{i'} p_0(\mathbf{x}, \mathbf{x}', t) * \hat{p}_{sc}(\mathbf{x}', \mathbf{x_s}, t) - \partial_{i'} \hat{p}_{sc}(\mathbf{x}', \mathbf{x_s}, t) * p_0(\mathbf{x}, \mathbf{x}', t)]n_i +$$
$$\int_V dV[(\lambda - \lambda_0)\partial_t \hat{p}(\mathbf{x}', \mathbf{x_s}, t) * \partial_t p_0(\mathbf{x}, \mathbf{x}', t) + \frac{(\rho - \rho_0)}{\rho\rho_0}\partial_{i'} \hat{p}_i(\mathbf{x}', \mathbf{x_s}, t) * \partial_{i'} p_{0i}(\mathbf{x}, \mathbf{x}', t)]. \tag{A.13}$$

The causal scattered wavefield p_{sc} is obtained by interchanging the role of the two wavefields in equation (A.8) by considering the anticausal state of p_0 instead of p. Following the same derivation as for the anticausal scattered wavefield yields:

$$p_{sc}(\mathbf{x}, \mathbf{x_s}, t) * \hat{h}(t) =$$
$$\int_S dS(\mathbf{x}')\rho^{-1}[\partial_{i'} \hat{p}_0(\mathbf{x}, \mathbf{x}', t) * p_{sc}(\mathbf{x}', \mathbf{x_s}, t) - \partial_{i'} p_{sc}(\mathbf{x}', \mathbf{x_s}, t) * \hat{p}_0(\mathbf{x}, \mathbf{x}', t)]n_i +$$
$$\int_V dV[(\lambda - \lambda_0)\partial_t p(\mathbf{x}', \mathbf{x_s}, t) * \partial_t \hat{p}_0(\mathbf{x}, \mathbf{x}', t) + \frac{(\rho - \rho_0)}{\rho\rho_0}\partial_{i'} p_i(\mathbf{x}', \mathbf{x_s}, t) * \partial_{i'} \hat{p}_{0i}(\mathbf{x}, \mathbf{x}', t)] \tag{A.14}$$

An anti causal wavefield emerge from the volume integral in equation (A.14) which cancel out the anti causal contribution from the surface integral in the same equation. This anti causal wavefield $\hat{p}_{sc}(\mathbf{x}, \mathbf{x_s}, t)$ is given as:

$$\hat{p}_{sc}(\mathbf{x}, \mathbf{x_s}, t) * h(t) =$$
$$\int_V dV[(\lambda_0 - \lambda)\partial_t \hat{p}(\mathbf{x}', \mathbf{x_s}, t) * \partial_t p_0(\mathbf{x}, \mathbf{x}', t) + \frac{(\rho - \rho_0)}{\rho\rho_0}\partial_{i'} \hat{p}(\mathbf{x}, \mathbf{x_s}, t) * \partial_{i'} p_0(\mathbf{x}, \mathbf{x}', t)]. \tag{A.15}$$

The sum of the causal scattered pressure and the anti causal scattered pressure is given by the sum $\Psi(\mathbf{x}, \mathbf{x_s}, tt)$:

$$\Psi(\mathbf{x}, \mathbf{x_s}, t) = p_{sc}(\mathbf{x}, \mathbf{x_s}, t) * h(t) - \hat{p}_{sc}(\mathbf{x}, \mathbf{x_s}, t) * \hat{h}(t) =$$
$$\int_S dS(\mathbf{x}')\rho^{-1}[\partial_{i'} \hat{p}_0(\mathbf{x}, \mathbf{x}', t) * p_{sc}(\mathbf{x}', \mathbf{x_s}, t) - \partial_{i'} p_{sc}(\mathbf{x}', \mathbf{x_s}, t) * \hat{p}_0(\mathbf{x}, \mathbf{x}', t)]n_i. \tag{A.16}$$

The sum Ψ states that the scattered wavefield p_{sc} due to a source at position $\mathbf{x_s}$ can be computed at any position $\mathbf{x}$ in volume V enclosed by the surface S if the scattered wavefield p_{sc} due to a source at $\mathbf{x_s}$ is known at position $\mathbf{x}'$ on S, as well as its normal derivative on S.

B Processing

Traveltime equations

The traveltime t from the source to the receiver via the reflector can be derived from Figure 5.1. From trigonometric identities, one gets:

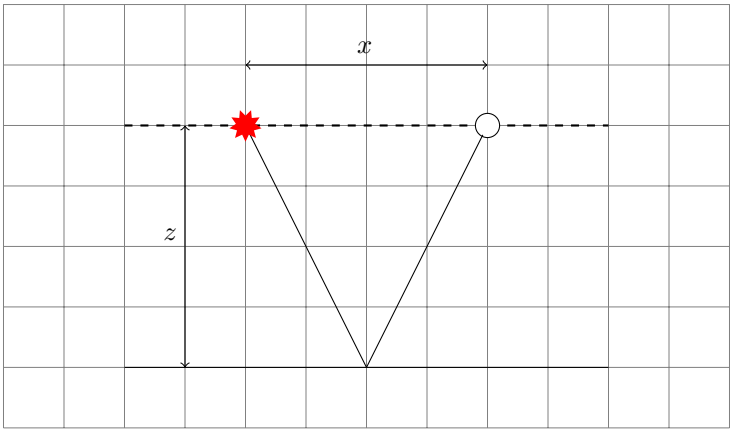

Figure 5.1: The seismic wave travels from the source to the reflection point at depth z and up again to the receiver at the surface.

$$(\frac{tv}{2})^2 = z^2 + (\frac{x}{2})^2, \tag{B.1}$$

where v is the wave velocity. The zero-offset two-way traveltime t_0 is given by: $t_0 = 2z/v$. Substituting t_0 into Equation (B.1) yields:

$$(\frac{tv}{2})^2 = (\frac{t_0 v}{2})^2 + (\frac{x}{2})^2. \tag{B.2}$$

which can be reduced to:

$$t = \sqrt{t_0^2 + (\frac{x}{v})^2}. \tag{B.3}$$

Equation (B.3) gives the traveltime for a horizontal reflector. For a dipping reflector, the geometry for the wave path is much more complicated than in the case of a horizontal reflector, see Figure 5.2. In order to derive a traveltime equation, a source ghost point $\mathbf{x_g}$ is introduced. The point lies a distance $2z$ from the source. The traveltime t for a dipping reflector can be derived as (Levin, 1971):

$$t = \sqrt{t_0^2 + (\frac{x}{v_{nmo}})^2}, \tag{B.4}$$

where v_{nmo} is the dip dependent apparent stacking velocity.

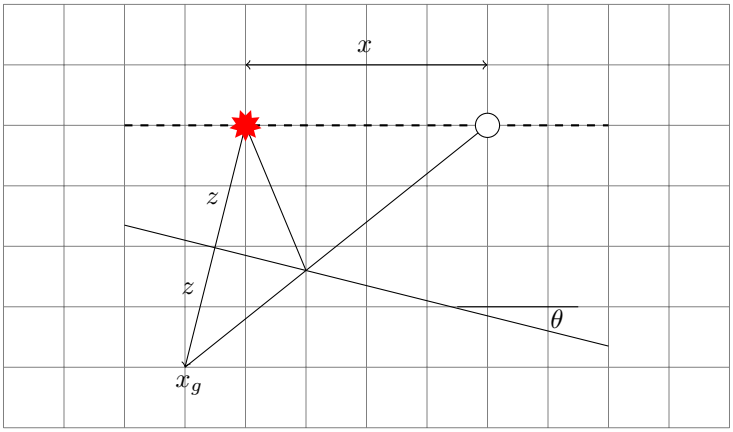

Figure 5.2: The seismic wave travels from the source to the reflection point and up again to the receiver. The reflector has a dip of angle θ.

CMP

A seismic experiment consists of large number of shot points where a seismic signal is emitted. Both source and receivers are moved between each shot point in order to increase the coverage area. The distance between shotpoints is small enough that the recorded area is covered multiple times, but with varying offset between source and receiver. In order to facilitate processing, the recorded data is sorted into common midpoint (CMP) gathers. In a CMP gather, a number of source and receivers pairs with variable offsets share a common midpoint, as can be seen in Figure 5.3. The midpoint lies on the surface halfway between the source and receiver. For a horizontal reflector, the reflection point lies vertically below the midpoint. In the case of a dipping reflector, the reflection point is moved updip from the point vertically below the midpoint, see Figure 5.4.

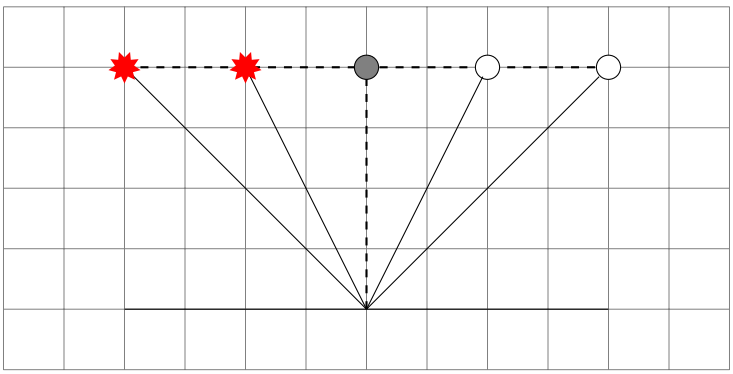

Figure 5.3: Common midpoint configuration, horizontal reflector. The common midpoint lies on the surface halfway between the source and the receiver. The subsurface reflection point is vertically below the midpoint.

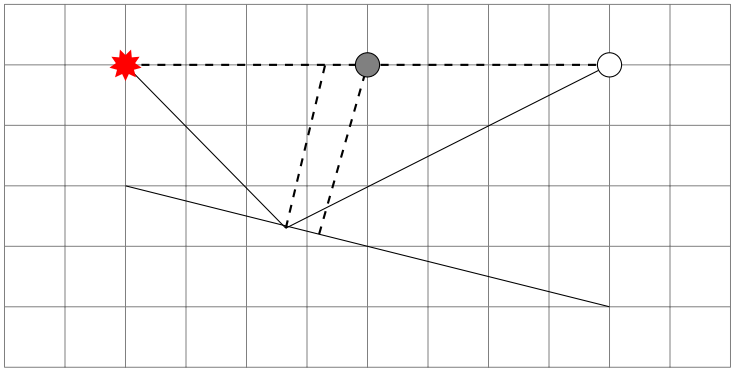

Figure 5.4: Common midpoint configuration, dipping reflector. The midpoint lies on the surface midway between the source and the receiver. Due to the dip of the reflector, the reflection point is not located vertically below the midpoint. Instead, it is moved updip compared to the midpoint.

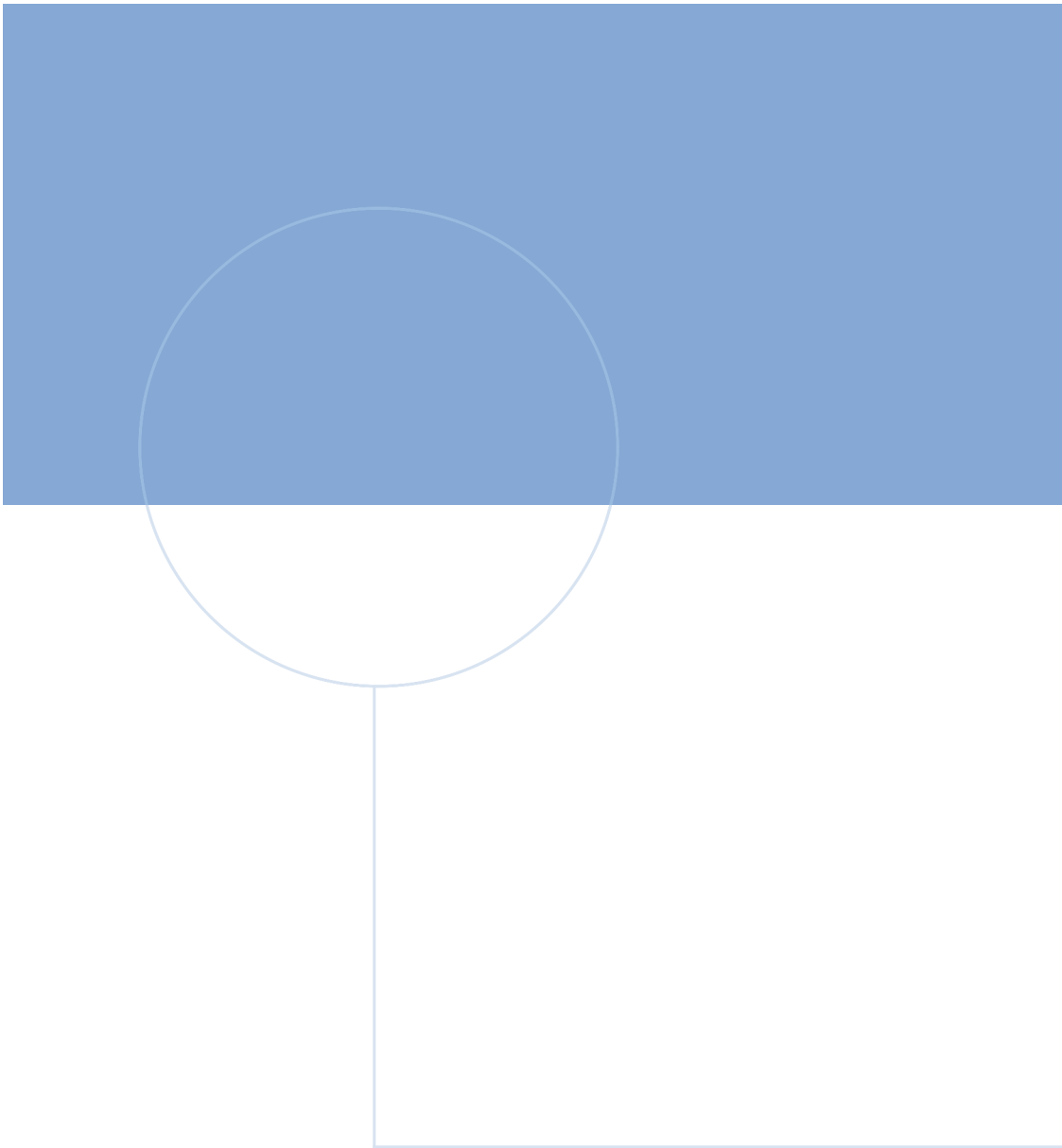

NTNU

Kunnskap for en bedre verden